Measuring and modeling investigation of the Net Photochemical Ozone Production Rate via an improved dual-channel reaction chamber technique

Yixin Hao[1,2#], Jun Zhou[1,2#*], Jie-Ping Zhou[1,2], Yan Wang[1,2], Suxia Yang[1,2], Yibo Huangfu[1,2], Xiao-Bing Li[1,2], Chunsheng Zhang[3], Aiming Liu[3], Yanfeng Wu[1,2], Yaqing Zhou, Shuchun Yang[1,2], Yuwen Peng[1,2], Jipeng Qi[1,2], Xianjun He[1,2], Xin Song[1,2], Yubin Chen[1,2], Bin Yuan[1,2*], Min Shao[1,2]

[1]Institute for Environmental and Climate Research, Jinan University, Guangzhou 511443, China

[2]Guangdong-Hongkong-Macau Joint Laboratory of Collaborative Innovation for Environmental Quality, Guangzhou 511443, China

[3]Shenzhen National Climate Observatory, Shenzhen 518040, China

[#]Yixin Hao and Jun Zhou contribute equally to this work.

Correspondence to: Jun Zhou (Junzhou@jnu.edu.cn) and Bin Yuan (byuan@jnu.edu.cn)

Abstract. Current process-based research mainly uses box models to evaluate the photochemical ozone production and destruction rates, and it is not clear to what extent the photochemical reaction mechanisms are understood. Here, we modified and improved a net photochemical ozone production rate (NPOPR, $P(O_3)_{net}$) detection system based on the current dual-channel reaction chamber technique, which makes the instrument applicable to different ambient environments, and its various operating indicators were characterized, i.e., the airtightness, light transmittance, wall losses of the reaction and reference chambers, conversion rate of O_3 to NO_2, air residence time, and performance of the reaction and reference chambers. The limits of detection of the NPOPR detection system were determined to be 0.07, 1.4, and 2.3 ppbv h^{-1} at sampling flow rates of 1.3, 3, and 5 L min^{-1}, respectively. We further applied the NPOPR detection system to field observations at an urban site in the Pearl River Delta (China). During the observation period, the maximum value of $P(O_3)_{net}$ was 34.1 ppbv h^{-1}, which was $\sim$ 0 ppbv h^{-1} at night within the system detection error and peaked at approximately noon local time. The daytime (from 6:00–18:00) average value of $P(O_3)_{net}$ was 12.8 ($\pm$5.5) ppbv h^{-1}. We investigated the detailed photochemical O_3 formation mechanism in the reaction and reference chambers of the NPOPR detection system using a zero-dimensional box model. We found that the photochemical reactions in the reaction chamber were very close to those in the ambient air, but it was not zero chemistry in the reference chamber, the reaction related to the production and destruction of RO_2 (=HO_2+RO_2) continued in the reference chamber, which

33 led to a small amount of $P(O_3)_{net}$. Therefore, the $P(O_3)_{net}$ measured here can be regarded as the lower

34 limit of the real $P(O_{3)net}$ in the atmosphere; however, the measured $P(O_3)_{net}$ was still $\sim$ 7.5 ppbv h^{-1} to 9.3

35 ppbv h^{-1} higher than the modeled $P(O_3)_{net}$ value depending on different modeling methods, which may

36 be due to the inaccurate estimation of HO_2/RO_2 radicals in the modeling study. Short-lived intermediate

37 measurements coupled with direct $P(O_3)_{net}$ measurements are needed in the future to better understand

38 O_3 photochemistry. Our results show that the NPOPR detection system can achieve high temporal

39 resolution and continuous field observations, which helps us to better understand photochemical O_3

40 formation and provides a key scientific basis for the continuous improvement of air quality in China.

41

42

1 Introduction

Surface O_3 pollution has become a major challenge in air quality management in China (Shen et al., 2021). Elevated surface O_3 mixing ratios exert severe adverse effects on public health, such as respiratory diseases, and the estimated annual mortality attributable to surface O_3 exposure is over 150,000 deaths in China (Malley et al., 2017). O_3 pollution is also detrimental to key staple crop yields, reducing the yields of wheat, soybean, and maize by up to 15 %, and is threatening global food security (Avnery et al., 2011; Mills et al., 2018; Karakatsani et al., 2010; Berman et al., 2012; O'Neill et al., 2003). As a greenhouse gas, O_3 also contributes significantly to climate change (Bell et al., 2004). With the rapid economic development and urbanization in the Pearl River Delta (PRD) region in China, O_3 pollution is pretty severe, especially in summer and autumn (Zou et al., 2015; Zhang et al., 2021).

The variation in O_3 in the planetary boundary layer is predominantly influenced by deposition, advection transport, vertical mixing (i.e., entrainment from the stratosphere), meteorological factors, and chemical reactions. Therefore, the O_3 budget in the boundary layer can be expressed as Eq. (1):

$$\frac{\partial [O_3]}{\partial t} = \underbrace{P(O_3) - D(O_3)}_{P(O_3)_{net}} \underbrace{- \frac{v}{H}[O_3]}_{SD} + \underbrace{u_i \frac{\partial [O_3]}{\partial x_i}}_{A} + STE \tag{1}$$

where SD, A, and STE represent the surface deposition, advection, and stratosphere-troposphere exchange (STE), respectively; $[O_3]$, $P(O_3)$ and $D(O_3)$ are the ambient O_3 mixing ratios, photochemical O_3 production and its loss rate, respectively; v, H, and u_i represent the O_3 deposition velocity, mixing layer height, and velocity in three directions, respectively; and A consists of u_i times the O_3 gradient in those three directions.

Tropospheric O_3 is a key component of photochemical smog, mainly formed by photochemical reactions of nitrogen oxides ($NO_x=NO+NO_2$) and volatile organic compounds (VOCs) (Lee et al., 2010). The specific process of the photochemical reaction is the photolysis of NO_2 at < 420 nm to generate $O(^3P)$ atoms, thereby promoting the formation of O_3 (Sadanaga et al., 2017). Simultaneously, there is a RO_X ($RO_X = OH + HO_2 + RO_2$) radical cycle in the troposphere, which continuously provides HO_2 and RO_2 to oxidize NO to NO_2 resulting in the accumulation of O_3 (Shen et al., 2021; Sadanaga et al., 2017; Cazorla et al., 2010).

Typical meteorological scenarios for the occurrence of O_3 pollution episodes in polluted urban

71 centers are usually characterized by weak winds, strong solar radiation, and high temperature (T). Under

72 such conditions, local formation of O_3 plays a crucial role in the rapid increase of surface O_3 in daytime.

73 In addition, in Eq. (1), the surface deposition and advection of O_3 are proportional to ambient O_3 mixing

74 ratios, $[O_3]$, which is mainly generated by local photochemistry (Carzorla et al., 2010). If $P(O_3)_{net}$ can be

75 reduced by regulatory measures, overall O_3 levels will decline proportionately over time (Cazorla et al.,

76 2010), thus, the investigation of $P(O_3)_{net}$ formation mechanism is urgently needed.

77   Current studies on $P(O_3)_{net}$ estimation mainly rely on modeling methods, the gas-phase chemical

78 mechanisms were frequently used to identify key drivers of O_3 pollution events and provide guidance for

79 making effective O_3 reduction strategies, such as the Master Chemical Mechanism (MCM), the regional

80 atmospheric chemistry mechanism (RACM), the Carbon Bond mechanisms (CBM) and the Mainz

81 Organic Mechanism (MOM) (Shen et al., 2021; Kanaya et al., 2016; Wang et al., 2014; Tadic et al.,

82 2020; Ren et al., 2013; Lu et al., 2010; Zhou et al., 2014; Mazzuca et al., 2016). However, uncertainties

83 in emission inventories, chemical mechanisms, and meteorology make it difficult to perfectly reproduce

84 real atmospheric processes, which can lead some bias in modeling the $P(O_3)_{net}$. According to the existing

85 field observations, researchers found that the mixing ratios of HO_2 or RO_2 obtained from the model

86 simulation was inconsistent with that obtained from the direct measurement, leading to the deviation of

87 $P(O_3)_{net}$ between observation and model simulation results (Wang et al., 2014; Tadic et al., 2020; Ren et

88 al., 2013; Martinez et al., 2003). Therefore, we urgently need a method that can directly measure the

89 $P(O_3)_{net}$.

90   Recently, researchers have developed sensors that can directly measure $P(O_3)_{net}$ in the atmosphere

91 using the dual-channel chamber technique (Sadanaga et al., 2017; Cazorla et al., 2010; Baier et al., 2015

92 and 2017; Sklaveniti et al., 2018), where ambient air is introduced into two chambers of identical size,

93 one UV transparent chamber (reaction chamber) and one UV protection chamber (reference chamber).

94 In the presence of solar UV light, O_3 is produced by photochemical reactions in the reaction chamber,

95 but not in the reference chamber. The system does not directly measure O_3 mixing ratios, it measures the

96 combined mixing ratios of O_3 and nitrogen dioxide (NO_2). $P(O_3)_{net}$ is determined by the difference of

97 O_X($O_X=O_3+NO_2$) mixing ratios between the reaction and reference chambers. These studies have greatly

98 helped us to understand the O_3 photochemical formation mechanism, but defects still exists in current

99 studies, for example, the sensors developed by Cazorla et al. (2010) and Baier et al. (2015) both have an

100 NO$_2$-to-O$_3$ converter unit, and uses a modified O$_3$ monitor (Thermo Scientific, Model 49i, USA) to

101 measure Ox, but the zero point of the O$_3$ monitor is easy to drift, together with the limitation of the

102 conversion efficiency of NO$_2$ to O$_3$ (~ 99.9 %) and the effects of the T and relative humidity (RH) to O$_3$

103 monitor, this method can introduce large measurement uncertainties. Sklaveniti et al. (2018) have shorten

104 the average residence time in the chambers to 4.5 min, which reduced the scattering and increased the

105 time resolution of ΔOx measurement, but large wall loss still exists in their system, which are 5 % and

106 3 % for O$_3$ and NO$_2$, respectively. Sadanaga et al. (2017) passed the NO standard gas into the PFA tube

107 to convert O$_3$ into NO$_2$ to detect Ox, which is easy to operate, but the LIF-NO$_2$ detector is less portable

108 and maintainable. Furthermore, all the current sensors have different degrees of wall loss of NO$_2$ and O$_3$

109 that can even reach 15 %, which largely affect the accuracy of the evaluation of $P(O_3)_{net}$.

110   In this study, we modified and improved the $P(O_3)_{net}$ sensor based on the dual-channel technique

111 as described above and named it the net photochemical ozone production rate (NPOPR) detection system.

112 Section 2 provides the improvement and characterization of the NPOPR detection system. Furthermore,

113 we applied the NPOPR detection system to an observation campaign conducted at Shenzhen

114 Meteorological Gradient Tower (SZMGT) in the Pearl River Delta (PRD) region in China. A zero-

115 dimensional box model based on the Framework for 0-D Atmospheric Modeling (F0AM) v3.2 coupled

116 with MCM v3.3.1 was used to simulate the photochemical reactions inside both the reaction and

117 reference chambers in the NPOPR system, which allowed us to assess the ability of the current modeling

118 method to model $P(O_3)_{net}$, as described in Sect. 3. The current research can help us to study the source

119 and formation mechanism of O$_3$ and provide effective theoretical support for the prevention and control

120 of O$_3$ pollution. Because the system can directly obtain real-time $P(O_3)_{net}$ under different environmental

121 conditions, it can meet richer and more specific research needs.

122 **2 Method and materials**

123 **2.1 Development of the NPOPR detection system**

124 The schematic and actual diagram of the NPOPR detection system are shown in Fig. 1. The integral

125 construction is similar to the $P\text{-}L(\text{Ox})$ measurement system built by Sadanaga et al. (2017) and Sklaveniti

126 et al. (2018), which mainly consists of reaction and reference chambers with the same geometry and

127 made of quartz (190.5 mm inner diameter and 700 mm length; more details can be found in Fig. S1). To

prevent photochemical reactions inside the reference chamber, an ultraviolet (UV) protection Ultem film

(SH2CLAR, 3 M, Japan) was used to cover the outer surface to block sunlight with wavelengths < 390

nm. During the experiment, both the reaction and reference chambers were located outdoors and exposed

to sunlight directly to simulate genuine ambient photochemistry reactions. Ambient air was introduced

into the reaction and reference chambers at the same flow rate, and a Teflon filter was mounted before

the chamber inlet to remove fine particles. A stream of air from the two chambers was alternately

introduced into an NO-reaction chamber every 2 min to convert O_3 in the air to NO_2 in the presence of

high mixing ratios of NO ($O_3+NO=NO_2$), and the Ox mixing ratios from the outlet NO-reaction chamber,

i.e., the total NO_2 mixing ratios including the inherent NO_2 in the ambient and that converted from O_3,

were measured by a Cavity Attenuated Phase Shift (CAPS) NO_2 Monitor (Aerodyne research, Inc.,

Billerica MA, USA) to avoid other nitrogen oxide interferences to the NO_2 measurement (such as alkyl

nitrates, peroxyacyl nitrates, peroxynitric acid, nitrogen pentoxide, etc.). Compared to previous studies

that used a dual-channel UV-absorption O_3 monitor (Cazorla et al., 2010) or the LIF-NO_2 monitor

(Sadanaga et al., 2017) for Ox measurements, our choice could make the NPOPR detection system have

a more stable zero-baseline and be more portable by assembling each part together, i.e., put the CAPS

NO_2 monitor, the automatic sampling system, and the automatic data sampling system onto the indoor

cabinets with the push-pull base, and put the dual chambers onto the outdoor shelf with the push-pull

base. Additionally, we modified the air sampling system to adjust the total air flow rates freely from 1.3

to 5 L min^{-1} in the reaction and reference chambers, which enabled us to achieve different air residence

times from 3.8 to 21 min. This time range covered all the residence times from previous studies using

different Ox measurement techniques, which ranged from 4.5 to 20.5 min (Cazorla et al., 2010; Baier et

al., 2015; Sadanaga et al., 2017; Sklaveniti et al., 2018). According to the simulation results described in

Sect. 3, the reaction rates of O_3 formation and destruction pathways and the radicals that play critical

roles in photochemical O_3 formation, such as HO_2, RO_2 and OH, reached quasi-steady states in

approximately 3 min, so it was reasonable for us to set the air flow rate highest at 5 L min^{-1}, where the

sampled air has already reacted for 3.8 min in the reaction and reference chambers. On the other hand,

this also demonstrated that it was reasonable to set the alternate sampling time for the reaction and

reference chambers at 2 min, where the sampled air actually has already reacted for at least 3.8 min in

the reaction and reference chambers. The switch system was controlled by two Teflon three-way solenoid

157 valves (001-0028-900, Parker, GER) located before the NO-reaction chamber (see Fig. 1). We used

158 homemade circuit control software (Four-Channel-Valves boxed) and a solenoid valve (001-0028-900,

159 Parker, GER) to automatically switch the sampling lines every 2 min. To keep the flow rates in the

160 reaction and reference chambers the same and avoid gas flow accumulation in the chamber, a pump

161 (pump 3) was connected to the Teflon three-way solenoid valves in parallel to the NO-reaction chamber

162 to evacuate the air that was not introduced into the NO-reaction chamber. To reduce NO interference, the

163 system used O_X to infer the amount of O_3 generated by photochemical reactions (Liu et al., 1977; Pan et

164 al., 2015; Lu et al., 2010). The difference in Ox mixing ratios in the reaction and reference chambers,

165 denoted by ΔOx, represents the amount of O_3 generated by the photochemical reaction. $P(O_3)_{net}$ was

166 obtained by dividing ΔOx by the average residence time of air in the reaction chamber $\langle \tau \rangle$:

167 $$P(O_3)_{net} = P(O_X) = \frac{\Delta O_X}{\tau} = \frac{[O_X]_{reaction} - [O_X]_{reference}}{\tau} \qquad (2)$$

168   Igor Pro version 6 was used to calculate $P(O_3)_{net}$ as follows: ① separate the data of the reaction

169 and the reference chambers into two sets using the recorded valve number of 1 (reaction chamber) and 0

170 (reference chamber) during the sampling time; ② for each 2 min period of data, delete the first 20 s and

171 the last 20 s when the signal was not stable, then average the rest data, and do the interpolate calculation

172 of the reference chamber dataset; ③ calculate the difference between the Ox mixing ratios in the reaction

173 and reference chambers (i.e., ΔO_X) at the time when the reaction chamber measured Ox; ④ divide ΔO_X

174 by the average residence time of air in the reaction chamber $\langle \tau \rangle$ and obtain $P(O_3)_{net}$ at a time resolution

175 of 4 min.

(a)

(b)
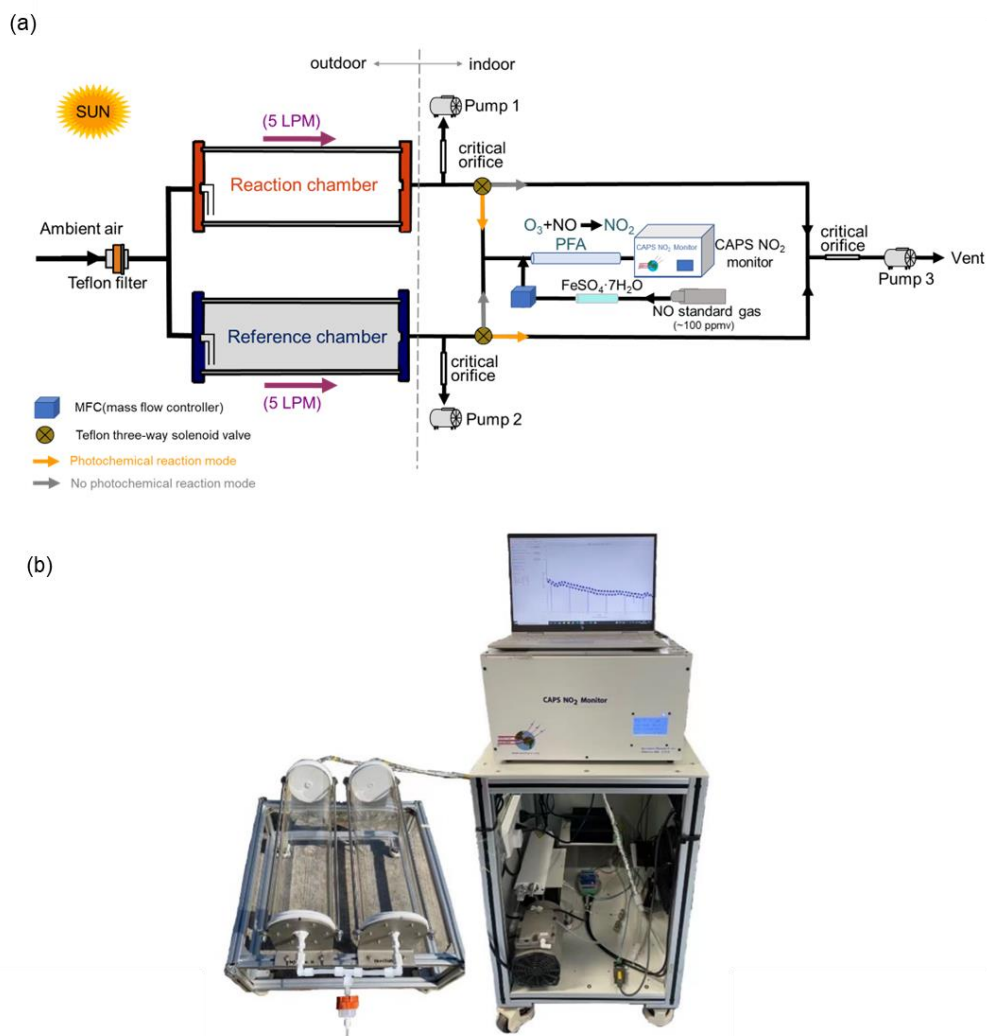
Figure 1: (a) Schematic and (b) actual diagram of the NPOPR detection system.

The major improvements of the NPOPR detection system described here compared to previous studies to optimize $P(O_3)_{net}$ measurements are as follows: (1) we improved the design of the reaction and reference chambers to ensure that they have good airtightness, which will increase the measurement accuracy of different species inside the chambers. More details can be found in Sect. 2.2 and Appendix I; (2) two pumps (labeled pump 1 and pump 2 in Fig. 1) were added directly after the reaction and reference chambers to continuously draw ambient air through the two chambers (as the makeup flow) to adjust the total air flow rates freely from 1.3 to 5 L min^{-1} in the chambers. By doing this, we were able to achieve different limits of detection (LODs) of the NPOPR system (see Sect. 2.4), making the instrument applicable to different ambient environments, i.e., in highly polluted areas, we could use higher air flow rates to reduce the wall loss effects of the chambers, and in less polluted areas, we could use lower flow rates to increase the instrument LOD. (3) We characterized the NPOPR detection system

189   at different air flow rates (including 1.3, 2, 3, 4, and 5 L min^{-1}) and tested the conversion efficiency of O_3

190   by NO to NO_2 in the NO-reaction chamber at different NO mixing ratios and NO-reaction chamber

191   lengths. These efforts enabled us to better understand the running parameters of the NPOPR system and

192   perform data corrections under different air flow rates (see Sect. 2.2); (4) we tested the performance of

193   both the reaction and reference chambers by combining the field measurements and MCM modeling,

194   which indicated that reaction pathways of $P(O_3)$ and $D(O_3)$ and the radicals that play critical roles in

195   photochemical O_3 formation, such as HO_2, RO_2 and OH, reached quasi-steady states in approximately 3

196   min, thus ensuring that the lowest air residence time of 3.8 min (at an air flow rate of 5 L min^{-1}) in the

197   reaction and reference chambers was long enough to obtain accurate $P(O_3)_{net}$ values (see Sect. 3.2). These

198   efforts made the NPOPR system less prone to biases than other systems and increased its applicability.

199   **2.2 Characterization of the NPOPR detection system**

200   We characterized the NPOPR detection system following the same procedures as previous researchers,

201   including the residence time of the air, the wall losses of NO_2 and O_3, the transmittance of light and

202   temperature differences in the reaction and reference chambers, and the quantitative conversion

203   efficiency of O_3 to NO_2 (α) in the NO-reaction chamber. Additionally, we investigated the residence time

204   of the air and the wall losses of NO_2 and O_3 in the reaction and reference chambers at different flow rates

205   (including 1.3, 2, 3, 4, and 5 L min^{-1}) and the conversion efficiency of O_3 by NO to NO_2 in the NO-

206   reaction chamber at different NO mixing ratios and NO-reaction chamber lengths. The detailed

207   experimental performances and data analysis are shown in Appendix I, and the corresponding results are

208   described as follows.

209   *The residence time.* We tested the residence time of air in both chambers under different air flow

210   rates, including 1.3, 2, 3, 4, and 5 L min^{-1}, the obtained related residence time in the reaction chamber

211   were 0.35, 0.16, 0.11, 0.07, and 0.06 h, respectively. By setting different air flow rates, we were able to

212   obtain different residence time thus different limit of detection of NPOPR system, which make it

213   applicable to different ambient environment. To make sure that the mean residence time of air is the same

214   in the reaction and reference chambers, we also tested the residence time of air in the reference chamber

215   in parallel, which were not much difference with that in the reaction chamber, as shown in Table S1. The

216   experimental schematic diagram is shown in Fig. S2, the related results of different air flow rates are

217   shown in Fig. S3 and Table S1.

218   ***Wall losses of NO₂ and O₃.*** At air flow rates of 1.3, 2, 3, 4, and 5 L min⁻¹, the wall losses of O_3 in

219   the reaction chamber were found to be approximately 2 %, 0 %, 0 %, 0 %, and 0 %, respectively, and the

220   wall losses of O_3 in the reference chamber were found to be approximately 2 %, 1 %, 1 %, 0 %, and

221   0.7 %, respectively. While the wall losses of NO_2 in the reaction chamber at air flow rates of 1.3, 2, 3, 4,

222   and 5 L min⁻¹ were found to be approximately 4 %, 4 %, 2 %, 0 %, and 0.3 %, respectively, the wall

223   losses of NO_2 in the reference chamber were found to be approximately 2 %, 1 %, 0 %, 0 %, and 0. 6 %,

224   respectively. The experimental schematic diagram is shown in Fig. S4, and the related results of different

225   air flow rates are shown in Figs. S5-S6 and Tables S2-S5. We further compared the wall losses of O_3 and

226   NO_2 in the reaction and reference chambers at 5 L min⁻¹ with previous studies (as shown in Table S6)

227   and found that they were significantly smaller, but even with a flow rate of 1.3 L min⁻¹, the wall losses

228   were still smaller than 4 % and 2 % in the reaction chamber and the reference chambers, respectively.

229   We also tested the wall losses of NO_2 and O_3 in the chamber at a 5 L min⁻¹ flow rate at different humidities

230   of 35-75 %, the detailed results are shown in Fig. S7 and S8, which shows that the variation in humidity

231   effected the wall loss of NO_2 and O_3 by 0.03-0.12 % and 1.06-1.19 %, respectively, which is much

232   smaller than the instrument detection error (which is 2 % at ambient NO_2 mixing ratios of 0-100 ppb),

233   which indicates the small effects of Ox loss on $P(O_3)_{net}$ measurements in our NPOPR detection system.

234   ***The light transmittance and temperature differences in the reaction and reference chambers.*** It

235   is worth noting that there was still low transmittance of light ranging from 390 nm to 790 nm through

236   the UV protection film, and the reference chamber could not be regarded as completely dark; thus, we

237   tested the solar UV transmittance through the reaction and reference chambers of the NPOPR detection

238   system in the laboratory using a sunlight simulation lamp (SERIC XG-500B, Japan) to provide different

239   intensities of illumination. The photolysis frequencies of NO_2, O_3, HONO, H_2O_2, NO₃_M (photolysis of

240   NO_3 generates NO+O_2), NO₃_R (photolysis of NO_3 generates NO_2+O), HCHO_M (photolysis of HCHO

241   generates H_2+CO), and HCHO_R (photolysis of HCHO generates H+HCO) inside and outside the

242   reaction and reference chambers were measured using an actinic flux spectrometer (PFS-100; Focused

243   Photonics Inc., China). Table 1 presents the $J(NO_2)$, $J(O^1D)$, and $J(HONO)$ results for the outside and

244   inside chambers from this study and from the literature. $J(H_2O_2)$, $J(NO_3\_M)$, $J(NO_3\_R)$, $J(HCHO\_M)$,

245   and $J(HCHO\_R)$ are shown in Table S7. The photolysis frequencies of all species inside the reaction

246 chamber were in agreement with those measured outside the reaction chamber within 4 %. For the

247 reference chamber, the transmittivities of $J(O^1D)$ and $J(NO_2)$ were ~ 2 % and 9 %, respectively, and the

248 transmittivities values of other species (i.e., $J(H_2O_2)$, $J(HCHO\_M)$ and $J(HCHO\_R)$, etc.) were almost

249 0 %. Specifically, the transmittivities of $J(NO_3\_M)$ and $J(NO_3\_R)$ of the reference chamber were more

250 than 90 % (Table S7). The influence of the different transmittivities of different species will be discussed

251 in Sect. 3. Table S7 shows that the transmittivities of $J(H_2O_2)$, $J(NO_3\_M)$, $J(NO_3\_R)$, $J(HCHO\_M)$, and

252 $J(HCHO\_R)$ in the reaction chamber were more than 90 %. Moreover, the transmittivities of $J(H_2O_2)$,

253 $J(HCHO\_M)$, and $J(HCHO\_R)$ of the reference chamber were almost 0 %, but the transmittivities of

254 $J(NO_3\_M)$ and $J(NO_3\_R)$ of reference chamber were more than 90 %. The reason for the lower HONO

255 transmittivities in the reference chamber than that of O_3 may be that the UV protection Ultem film on the

256 reference chamber blocks sunlight at wavelengths < 390 nm, where the spectral atlas of HONO was

257 under wavelengths of 190-395 nm at 298 K, while that of O_3 was under wavelengths of 410-750 nm at

258 298 K (IUPAC, 2004, http://iupac. pole-ether.fr/).

259 **Table 1. Photolysis frequency J (s^{-1}) of different species inside and outside the reaction and reference chambers.**
260 **The shaded and clear regions correspond to the photolysis frequencies with the reference (Ultem coated) and**
261 **reaction (clear) chambers, respectively. The transmittivities column shows the transmittivities of the tested**
262 **chamber measurements with the set photolysis frequencies using SERIC XG-500B sunlight (this study) and**
263 **ambient (literature).**

	Transmittivities			
	Averaged (this study)	Cazorla et al., 2010	Baier et al., 2015	Sadanaga et al., 2017
$J(NO_2)$	0.985 ±0.037	0.974	0.990	0.986
	0.094 ±0.014	0.021	0.01	0.121
$J(O^1D)$	1.020 ±0.04	0.991	0.978	1.030
	0.019 ±0.011	0.0058	0.001	~0
$J(HONO)$	0.983 ±0.037	0.976	0.982	0.988
	0.002 ±0.0002	0.0067	~0	0.017

264

265   We further detected the temperature in both the reaction and reference chambers when running the

266 NPOPR system in an ambient observation campaign during November 2022 on the Panyu campus of

267 Jinan University in Guangzhou, China (113° 36′ E, 23° 02′ N). We found that the UV protection

268 Ultem film on the reference chamber did not block the heat outside the chamber, and the temperature

269 remained the same in the reaction and reference chambers during the measurement test, as shown in Fig.

270 S10.

271 ***The quantitative conversion efficiency of O_3 to NO_2 (α)*** in the NO-reaction chamber is crucial for

272 accurate measurement of $P(O_3)_{net}$. Here, we used a perfluoroalkoxy (PFA) tube (outer diameter of 12.7

273 mm; inner diameter of 9.5 mm) as the NO-reaction chamber. The experimental schematic diagram is

274 shown in Fig. S12. Known mixing ratios of O_3 and NO standard gas were introduced into the NO-reaction

275 chamber, and NO reacted with O_3 to produce NO_2. To avoid the influence of small amounts of NO_2

276 impurity in the NO standard gas used for conversion, we added a cylinder filled with partialized crystals

277 of $FeSO_4 \cdot 7H_2O$ to reduce NO_2 in the NO/N_2 gas cylinder to NO. We injected ~1800 ppbv NO into the

278 NO-reaction chamber and tested the NO_2 mixing ratios from its outlet using a CAPS NO_2 monitor, as

279 shown in Fig. S13. We found that the standard deviation of the NO_2 mixing ratios was lower than 0.027

280 ppbv, which is smaller than the baseline drifts of the CAPS (which were 0.043 and 0.030 ppbv (1 σ) at

281 integration times of 35 and 100 s, respectively, as mentioned in Sect. 2.3), so we believe the particulate

282 crystals of $FeSO_4 \cdot 7H_2O$ performed well and the potential bias introduced by the impurity in NO mixing

283 ratio for $P(O_3)_{net}$ was negligible. Finally, the total NO_2 mixing ratios, including that from the ambient air,

284 were measured using a CAPS NO_2 monitor ($[NO_2]_{CAPS}$). The O_3 mixing ratios were controlled at

285 approximately 310 ppbv according to the maximum mixing ratio range in the normal ambient atmosphere

286 (to ensure that all ambient and newly generated O_3 can react with NO and produce equivalent amounts

287 of NO_2). An O_3 generator equipped with a low-pressure mercury lamp was employed to generate O_3, and

288 the generated O_3 mixing ratios ($[O_3]_g$) were measured by a 2B O_3 monitor as mentioned above. Here, we

289 note that the O_3 mixing ratios were diluted by the added NO/N_2 gas (with a flow rate of 20 mL min^{-1}) in

290 the NO-reaction chamber (with a total flow rate of 1.11 L min^{-1}), taking 1800 ppbv NO/N_2 gas as an

291 example, the relationship between $[NO_2]_{CAPS}$ and $[O_3]_g$ can be described by Eq. (3):

292 $$[NO_2]_{CAPS} = \frac{1.09}{1.11}[O_3]_g \alpha \qquad (3)$$

293 To determine the optimal length of the NO-reaction chamber and NO mixing ratios, we performed

294 a cross test of α under the following scenarios: the NO-reaction chamber lengths were increased from 30

295 to 650 cm in 50 cm steps, and the NO standard gas (102.1 ppmv) was diluted to 600, 900, 1200, 1500,

296 1800, 2100, and 2400 ppbv in the NO reaction chamber. The results are shown in Fig. 2. We found that

297 at $[O_3]_g$ of approximately 310 ppbv, with NO mixing ratios $\geq$1800 ppbv in the NO reaction chamber, α

298   reached 99 %, 99.6 %, and 99.9 % with NO-reaction chamber lengths of 50, 70, and 100 cm, respectively,

299   where the corresponding O_3 residence times in the NO reaction chamber were 1.95, 2.74, and 3.91 s,

300   respectively. Considering both the optimal reaction time in the NO reaction chamber and α, we selected

301   the NO reaction chamber length as 100 cm with an NO mixing ratio of 1800 ppbv for the NPOPR

302   detection system.
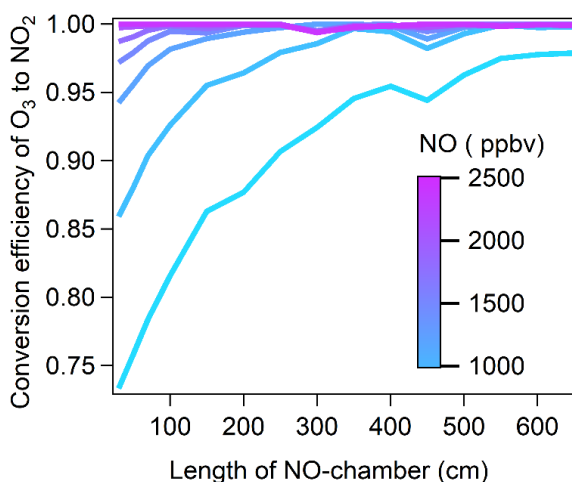
303

304   **Figure 2: The conversion efficiency of O_3 by NO to NO_2 in the NO reaction chamber as a function of the NO**
305   **chamber length, color coded by the NO mixing ratios.**

306   ***The airtightness of the reaction and reference chambers*** We also checked the airtightness of the

307   reaction and reference chambers by passing through gases with different flow rates based on the

308   schematic diagram shown in Fig. S14 and compared the values of [air flow rate × pressure] between the

309   inlet and outlet of the chambers (as indicated in Fig. 3). We found that the deviations in [air flow rate ×

310   pressure] at the inlet and outlet of the reaction and reference chambers at different flow rates were <3 %

311   (as shown in Table S8), indicating the good airtightness of the reaction and reference chambers. This

312   ensured that the photochemical reactions in the reaction and reference chambers would not be affected

313   by the ambient air outside the chambers.

314

315
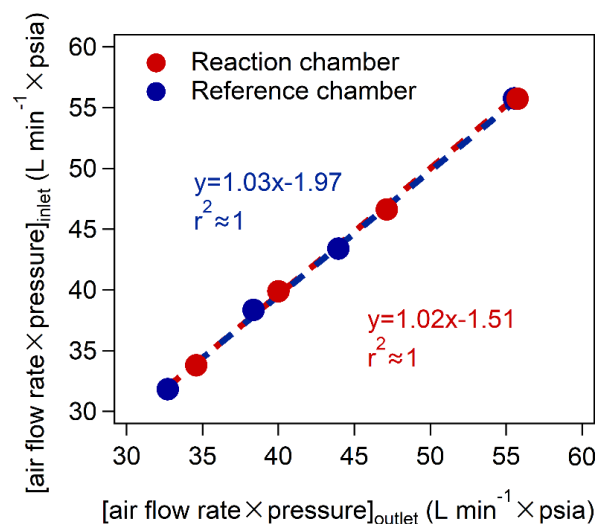
Figure 3: The relationship of the values of [air flow rate × pressure] between the inlet and outlet of the chambers (psia: Pounds Per Square Inch Absolute).

The flow states in the reaction and reference chambers We calculated the Reynolds number to check the gas flow state in the reaction and reference chambers. The Reynolds number (expressed as Eq. (4)) is a dimensionless number that can be used as the basis for judging the flow characteristics of a fluid:

$$Re = \rho v d / \mu \tag{4}$$

where v, ρ and μ are the flow velocity, density and viscosity coefficient of the fluid, respectively. In this study, the fluid is air, and d is the equivalent diameter of the reaction and reference chambers. The calculated Reynolds numbers in the two chambers under flow rates of 1.3, 2, 3, 4, and 5 L min^{-1} were 9.39, 14.58, 21.75, 29.05, and 36.34, respectively, indicating laminar flows in both chambers at different flow rates.

The HONO production in the reaction and reference chambers We tested the HONO production in the reaction and reference chambers under weather conditions similar to those during the SZMGT observations (humidity of 60-90% at a temperature of ∼ 20 °C and $J(NO_2)$ of ∼ 0-8 × 10^{-3} s^{-1}) at a 5 L min^{-1} sampling flow rate. We found that the HONO mixing ratios in the reaction and reference chambers were almost the same and not statistically different from that in the ambient air within the standard deviation, as shown in Fig. S9; therefore, we assumed that the HONO production in the reaction and reference chambers would not cause a significant difference in $P(O_3)_{net}$ in the two chambers. Unfortunately, we did not test HONO during the field observation period, but we have added the modeled HONO produced from the precursors before the ambient air was injected into the NPOPR system, as

337 described in Sect. 3.2.

2.3 Calibration and measurement error of the CAPS NO$_2$ monitor

339 The Ox in the NPOPR detection system was measured by the CAPS NO$_2$ monitor. Detailed descriptions

340 of this technique can be found elsewhere (Kebabian et al., 2008, 2005). We calibrated the CAPS NO$_2$

341 monitor using a NO$_2$ standard gas (with an original mixing ratio of 2.08 ppmv), which was first calibrated

342 using the gas-phase titration method using NO standard gas and excessive O$_3$. The related experimental

343 results are shown in Fig. S15. The detailed calibration procedure is as follows: a. injected ~ 10–100 ppbv

344 of NO$_2$ standard gas for 30 min to passivate the surfaces of the monitor and then injected dry pure air for

345 ~ 10 min to minimize the zero point drift, which were 0.043 and 0.047 ppbv at integration times of 35

346 and 100 s, respectively, and resulted in LODs of CAPS of 0.13 and 0.14 ppbv (3 σ), respectively; b.

347 injected a wide range of NO$_2$ mixing ratios (from 0–160 ppbv) prepared by mixing the NO$_2$ standard gas

348 with ultrapure air into the CAPS NO$_2$ monitor and repeated the experiments three times at each NO$_2$

349 mixing ratio. The final results are shown in Fig. 4. To check the baseline drift of the CAPS at different

350 humidities, we added another two sets of tests (as shown in Fig. S11) using ambient air and wet pure air

351 and found that (a) when injecting ambient air into the CAPS (RH ranged from ~30-35%), the baseline

352 drifts were 0.035 and 0.032 ppbv (1 σ) at integration times of 35 and 100 s, respectively; and (b) when

353 injecting wet pure air into the CAPS (RH ranged from 35-70%), the baseline drifts were 0.043 and 0.030

354 ppbv (1 σ) at integration times of 35 and 100 s, respectively. These baseline drifts were smaller than those

355 when injecting dry pure air to estimate the LOD of the CAPS. We chose the largest baseline drift when

356 injecting dry pure air to estimate the $P(O_3)_{net}$ error in the following analysis; by doing this, we were able

357 to include all the short-duration baseline drifting in the CAPS NO$_2$ monitor under different humidities.

358 To obtain an accurate measurement error of the CAPS NO$_2$ monitor (($O_{X_{CAPS}})_{error}$), we fitted the

359 calibration results with a 68.3 % confidence level, and the blue line in Fig. 4 represents the maximum

360 fluctuation range under this confidence level. ($O_{X_{CAPS}})_{error}$ was then calculated from the fluctuation

361 range of the 68.3 % confidence interval of the calibration curve. The relationship between ($O_{X_{CAPS}})_{error}$

362 and the measured Ox value ($[Ox]_{measured}$) can be expressed as a power function curve, as shown in Eq.

363 (5):

364 $(O_{X_{CAPS}})_{error} = 9.72 \times [O_X]_{measured}^{-1.0024}$ (5)

365    Subsequent $P(O_3)_{net}$ error estimation according to the instrument measurement error of the CAPS

366  NO_2 monitor and the O_3 light-enhanced loss in the reaction and reference chambers are described in

367  Appendix II.
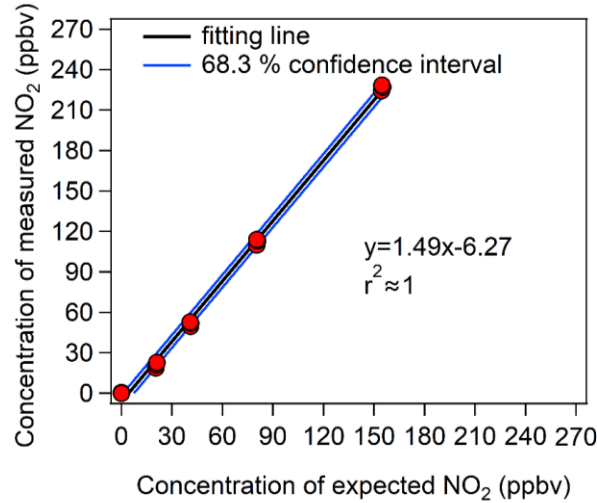
368

369  **Figure 4: Calibration results of the CAPS NO_2 monitor with different NO_2 mixing ratios. The y-axis represents**

370  **the NO_2 mixing ratios measured by the CAPS NO_2 monitor, and the x-axis represents the prepared NO_2**

371  **mixing ratios from the diluted NO_2 standard gas.**

372  **2.4 The measurement error of $P(O_3)_{net}$ and the LOD of the NPOPR detection system**

373  To assess the measurement error of $P(O_3)_{net}$ and the LOD of the NPOPR detection system, dry pure air

374  was introduced into the NPOPR detection system in sequence to adjust the system for ~ 2 h, followed by

375  dry pure air or ambient air when the time resolution of the CAPS NO_2 monitor was 1 s and the integration

376  time period was 100 s (the measurement durations for the reaction and reference chambers were both 2

377  min). The LOD of the NPOPR detection system was obtained as three times the measurement error of

378  $P(O_3)_{net}$, which was determined at a time resolution of 4 min by propagating the errors of the Ox measured

379  by the CAPS NO_2 monitor when ultrapure air or ambient air was introduced into the NPOPR detection

380  system, combined with the related $\langle\tau\rangle$ under different flow rates, i.e., $\langle\tau\rangle$ was 0.063 h at a flow rate of 5

381  L min^{-1}. The detailed calculation method is shown in Eq. (6):

382  $$LOD = \frac{3 \times \sqrt{([O_X]_{rea\_std})^2 + ([O_X]_{ref\_std})^2}}{\tau}$$   (6)

383  where $[O_X]_{rea\_std}$ and $[O_X]_{ref\_std}$ represent the standard deviation of O_X in the reaction and reference

384  chambers measured by the CAPS NO_2 monitor with an integration time period of 100 s, respectively.

385   However, considering that the background Ox mixing ratios (measured by the CAPS NO_2 monitor

386   of the air in the reference chamber) changed when measuring the ambient air, the measured O_X errors in

387   the reaction and reference chambers changed with the Ox mixing ratios (as shown in Sect. 2.3), and the

388   LOD must also be a function of the intrinsic ambient and photochemically formed O_3 and NO_2 mixing

389   ratios (i.e., the Ox mixing ratios measured by the CAPS NO_2 monitor). It is worth noting that the

390   measured O_X errors may also be influenced by the light-enhanced loss of O_3 in the reaction and reference

391   chambers under ambient conditions when the light intensity (especially $J(O^1D)$) and O_3 mixing ratios are

392   high, as tested and shown in Appendix II, but this effect is included in the measured O_X errors. Therefore,

393   when injecting ambient air into the NPOPR system, the error and LOD of $P(O_3)_{net}$ with a residence time

394   of τ can be calculated using Eq. (7) and Eq. (8), respectively:

395    $$P(O_3)_{net\_error}=\frac{\sqrt{(O_{X_\gamma})_{rea\_error}^2+((9.72\times[O_X]_{rea\_measured}^{-1.0024}))_{rea\_std}^2+(O_{X_\gamma})_{ref\_error}^2+((9.72\times[O_X]_{ref\_measured}^{-1.0024}))_{ref\_std}^2}}{\tau} \qquad (7)$$

396    $LOD= 3\times P(O_3)_{net\_error}$ (8)

397   where $(O_{X_\gamma})_{rea\_error}$ and $(O_{X_\gamma})_{ref\_error}$ represent the measurement error caused by the light-enhanced loss

398   of O_3 in the reaction and reference chambers, respectively, and $(9.72\times[O_X]_{measured}^{-1.0024})_{rea\_std}$ and

399    $(9.72\times[O_X]_{measured}^{-1.0024})_{ref\_std}$ represent the standard deviation of O_X in the reaction and reference

400   chambers caused by the CAPS NO_2 monitor with an integration time period of 100 s, respectively. More

401   details about the $(O_{X_\gamma})_{rea\_error}$ and $(O_{X_\gamma})_{ref\_error}$ estimation method can be found in Appendix II.

402   In conclusion, the LOD of the NPOPR detection system is determined to be three times $P(O_3)_{net\_error}$,

403   where $P(O_3)_{net\_error}$ is mainly determined by the measurement error of Ox (including the Ox measurement

404   error of the CAPS NO_2 monitor, the light-enhanced loss of O_3, and the chamber Ox losses). Because the

405   measurement error of the CAPS NO_2 monitor decreases with increasing Ox mixing ratios (as shown in

406   Sect. 2.3), higher LODs could be obtained when injecting dry pure air into the NPOPR detection system,

407   which were approximately 0.07, 1.4, and 2.3 ppbv h^{-1} at air flow rates of 1.3, 3, and 5 L min^{-1}, respectively.

408   The results are summarized in Table S9.

409   During the field observations, the LOD values were highly dependent on the ambient conditions,

410   especially the light intensity and the Ox mixing ratios, and higher O_3 mixing ratios and lower light

411   intensity will likely result in lower LOD values.

 2.5 Laboratory tests of the NPOPR detection system

413 We conducted an experiment in the laboratory to test the performance of the NPOPR detection system at

414 Jinan University Panyu Campus (23.0° N, 113.4° E) on 26 March 2021. Ambient air (5 L min^{-1}) was

415 simultaneously injected into the reaction and reference chambers of the NPOPR detection system in

416 parallel, and the sunlight simulation lamp mentioned above was used to simulate sunlight radiation. The

417 light intensities of the sunlight simulation lamp were decreased from 26000 cd to 0 cd in steps of 3700

418 cd, where cd indicates the light intensity SI unit candela. $P(O_3)_{net}$ was 28.6 ppbv h^{-1} at a light intensity of

419 26000 cd and gradually approached 0 ppbv h^{-1} at 0 cd (as shown in Fig. 5), indicating that the $P(O_3)_{net}$

420 change due to the different sunlight radiation could be well captured by the NPOPR detection system.
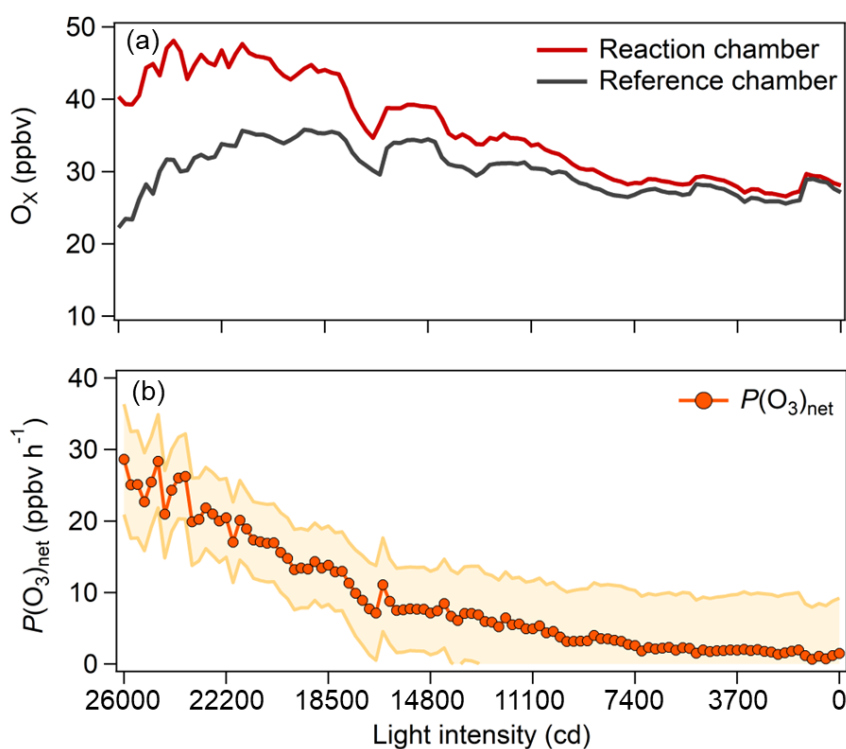
421

422 **Figure 5: (a) Measured Ox mixing ratios in the reaction and reference chambers and (b) the related $P(O_3)_{net}$**

423 **as a function of the light intensity during the experiment.**

424 **3 Atmospheric study and discussion**

425 **3.1 Field observations**

426 The self-built NPOPR detection system was employed in the field campaign conducted at SZMGT, which

427 is located in Shenzhen, China (as shown in Fig. S17), from 7 to 9 December 2021. During the campaign,

428   to achieve the lowest O_3 and NO_2 wall loss, we used a 5 L min^{-1} air flow rate in the reaction and reference

429   chambers (with a residence time of ~ 4 min). The photolysis frequencies of different species were

430   measured using the actinic flux spectrometer as mentioned above. O_3 and NO_X ($NO+NO_2$) mixing ratios

431   were measured using a 2B O_3 monitor and a chemiluminescence NOx monitor (Model 42i, Thermo

432   Fisher Scientific, USA), respectively. T and RH were measured by a portable weather station (Met Pak,

433   Gill Instruments Ltd, UK). Volatile organic compounds (VOCs) were measured by high-resolution

434   proton transfer reaction time-of-flight mass spectrometry (PTR-ToF-MS, Ionicon Analytik, Austria)

435   (Wang et al., 2020a; Wu et al., 2020) and an off-line gas chromatography mass spectrometry flame

436   ionization detector (GC–MS-FID) technique (Wuhan Tianhong, Co. Ltd, China) (Yuan et al., 2012)

437   (Table S11). Additionally, a self-built formaldehyde analyzer was used to detect formaldehyde (HCHO)

438   (Zhu et al., 2020). Figure 6 presents the temporal and diurnal variations in the $P(O_3)_{net}$, O_X, O_3, NO,

439   NO_2, NO_X, T, RH, $J(O^1D)$, and $J(NO_2)$ mixing ratios at SZMGT during the campaign.
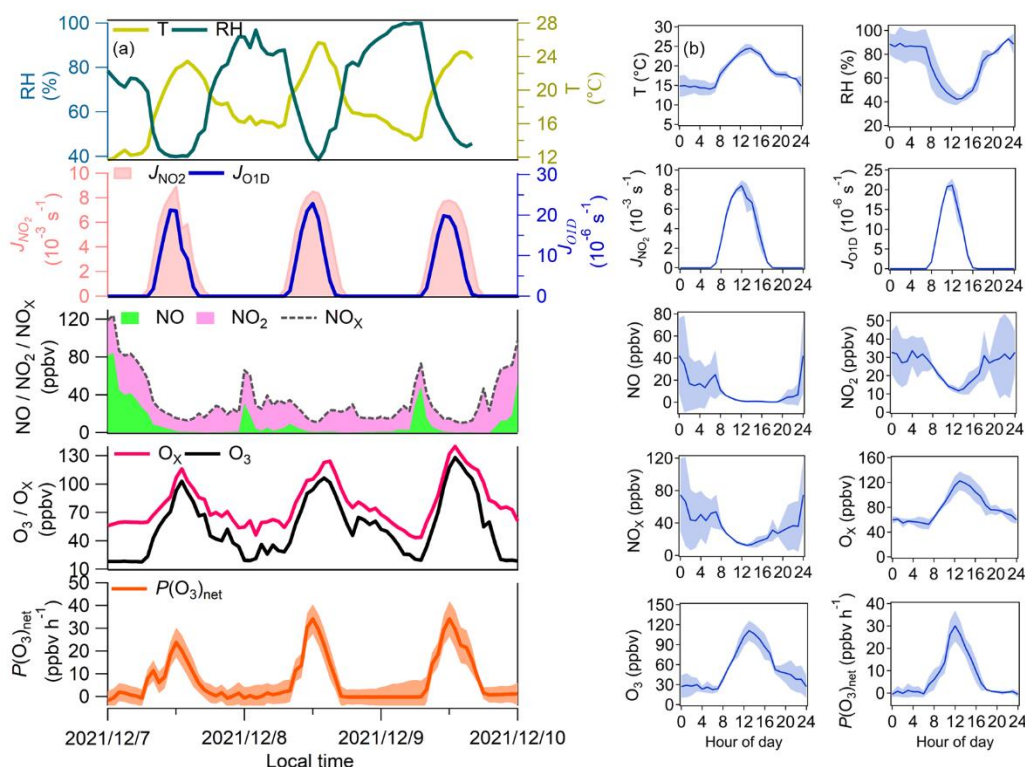
440

441   **Figure 6: (a) Time series and (b) average diurnal variations of $P(O_3)_{net}$, $J(NO_2)$, $J(O^1D)$, T, RH, O_X, NO_2 and**

442   **NO measured at SZMGT from 7 to 9 December 2021. The shaded areas represent the error of each measured**

443   **species, where the error of $P(O_3)_{net}$ was calculated according to the method described in Appendix II (the**

444   **estimation of the $P(O_3)_{net}$ error).**

445

446   During the measurement period, $P(O_3)_{net}$ ranged from ~ 0 to 34.1±7.8 ppbv h^{-1}, with an average

447 daytime (from 6:00–18:00) value of 12.8 (±5.5) ppbv h^{-1}. The maximum $P(O_3)_{net}$ at SZMGT was lower

448 than that measured in the urban area of Houston in the US (40–50 ppbv h^{-1} and 100 ppbv h^{-1} in autumn

449 and spring, respectively) (Baier et al., 2015; Ren et al., 2013), close to that measured in Indiana in the

450 US (~ 30 ppbv h^{-1} in spring) (Sklaveniti et al., 2018), and much higher than that measured at the

451 Wakayama Forest Research Station, a remote area of Japan (10.5 ppbv h^{-1} in summer) (Sadanaga et al.,

452 2017) and an urban area of Pennsylvania in the US (~ 8 ppbv h^{-1} in summer) (Cazorla et al., 2010). The

453 result indicates the rationality of the measured $P(O_3)_{net}$ in this study. From previous studies, the O_3

454 pollution in the PRD area is more severe in summer and autumn than in winter and spring (Zhang et al.,

455 2021). In this study, $P(O_3)_{net}$ was measured in wintertime, which was already high, so we believe that the

456 O_3 pollution of the PRD is severe and urgently needs to be controlled. More measurements of $P(O_3)_{net}$

457 worldwide are listed in Table S10, and we found that $P(O_3)_{net}$ was much higher in urban areas than in

458 remote areas using both modeling and direct measurement methods.

459 According to the diurnal variation in all the measured pollutant indicators, $P(O_3)_{net}$ started to

460 increase at approximately 7:00 local time, which may be due to two reasons: (1) the rise in O_3 precursors

461 (i.e., VOCs) due to the high-altitude atmospheric residual layer transported downward near the surface

462 at this time and (2) the increase in solar radiation intensity after 7:00, which increased the oxidation

463 capacity of the pollutants. These two factors jointly enhanced the photochemical oxidation reaction of

464 VOCs and gradually increased $P(O_3)_{net}$. $P(O_3)_{net}$ then peaked at approximately 12:0, which was consistent

465 with $J(NO_2)$, but this peak time was earlier than that of O_3, which peaked at approximately 14:00 , which

466 may be due to the photochemical reactions dominating O_3 mixing ratio changes between 12:00 and 14:00 .

467 After 14:00, the O_3 mixing ratios started to decrease, which may be due to other processes dominating

468 O_3 mixing ratio changes at this time, such as O_3 reacting with other pollutants or surface deposition and

469 the outflow of O_3 by physical transport. In conclusion, changes in O_3 mixing ratios were influenced by

470 both photochemical production and physical transport. Because HO_2 and RO_2 were not well captured in

471 the model, the simulations could lead to an underestimation of $P(O_3)_{net}$.

472 **3.2 Model simulation of $P(O_3)_{net}$ in the reaction and reference chambers**

473 **3.2.1 Modeling method**

474 To obtain a comprehensive understanding of the ozone production rate $P(O_3)$ and ozone destruction rate

475 $D(O_3)$ during the 4-min photochemical reaction in the reaction and reference chambers, we modeled

476   *P*(O$_3$) and *D*(O$_3$) at 12:00 on 7 December 2021 based on field observation data using a zero-dimensional

477   box model based on the Framework for 0-D Atmospheric Modeling (F0AM) v3.2 coupled with MCM

478   v3.3.1, which contains a total of 143 VOCs, more than 6700 species, involving more than 17000 reactions

479   (Jenkin et al., 2015). *P*(O$_3$)$_{net}$ can be expressed by the difference between *P*(O$_3$) and *D*(O$_3$), and *P*(O$_3$)

480   and *D*(O$_3$) can be expressed as Eq. (9)–(10).

481     $P(O_3)=k_{HO_2+NO}[HO_2][NO]+\sum_i k_{RO_{2,i}+NO}[RO_{2i}][NO]\varphi_i$ (9)

482     $D(O_3)=k_{O(^1D)+H_2O}\left[O\left(^1D\right)\right][H_2O]+k_{OH+O_3}[OH][O_3]+k_{HO_2+O_3}[HO_2][O_3]$

483        $+\sum_i \left(k_{O_3+Alkene_i}[O_3][Alkene_i]\right)+k_{OH+NO_2}[OH][NO_2]+k_{RO_{2,i}+NO_2}[RO_{2i}][NO_2]$ (10)

484   where k_{M+N} represents the bimolecular reaction rate constant of M and N, and φ_i is the yield of NO$_2$ from

485   the reaction RO$_{2i}$ +NO. The relevant reaction rates of *P*(O$_3$) and *D*(O$_3$) and the VOCs mixing ratios during

486   7–9 December 2021 in SZMGT used in the model are listed in Tables 2 and S11.

487

488   **Table 2. O$_3$ production and destruction reactions and the relevant reaction rates used in the model.**

Reactions	Rate coefficient / unit	Number
O$_3$ production pathways - *P*(O$_3$)		
RO$_2$+ NO→RO + NO$_2$	$2.7\times10^{-12}\times\exp(360/T)$ / molecules $^{-1}$ cm^3 s^{-1}	(R1)
HO$_2$+ NO→OH + NO$_2$	$3.45\times10^{-12}\times\exp(270/T)$ / molecules $^{-1}$ cm^3 s^{-1}	(R2)
O$_3$ loss pathways - *D*(O$_3$)		
O$_3$ + hv → O^{1}D + O$_2$	Measured JO^1D / s^{-1}	(R3)
O$_3$ + C$_2$H$_4$ → HCHO + CH$_2$OOA	$9.1\times10^{-15}\times\exp(-2580/T)$ / molecules $^{-1}$ cm^3 s^{-1}	(R4)
O$_3$ + C$_3$H$_6$ → CH$_2$OOB + CH$_3$CHO	$2.75\times10^{-15}\times\exp(-1880/T)$ / molecules $^{-1}$ cm^3 s^{-1}	(R5)
O$_3$ + C$_3$H$_6$ → CH$_3$CHOOA + HCHO	$2.75\times10^{-15}\times\exp(-1880/T)$ / molecules $^{-1}$ cm^3 s^{-1}	(R6)
O$_3$ + C$_5$H$_8$ → CH$_2$OOE + MACR	$3.09\times10^{-15}\times\exp(-1995/T)$ / molecules $^{-1}$ cm^3 s^{-1}	(R7)
O$_3$ + C$_5$H$_8$ → CH$_2$OOE + MVK	$2.06\times10^{-15}\times\exp(-1995/T)$ / molecules $^{-1}$ cm^3 s^{-1}	(R8)
O$_3$ + C$_5$H$_8$ → HCHO + MACROOA	$3.09\times10^{-15}\times\exp(-1995/T)$ / molecules $^{-1}$ cm^3 s^{-1}	(R9)
O$_3$ + C5H$_8$ → HCHO + MVKOOA	$2.06\times10^{-15}\times\exp(-1995/T)$ / molecules $^{-1}$ cm^3 s^{-1}	(R10)
O$_3$+ HO$_2$ → OH	$2.03\times10^{-16}\times (T/300)^{4.57}\exp(693/T)$ / molecules $^{-1}$ cm^3 s^{-1}	(R11)
RO$_2$+ NO$_2$ → peroxy nitrates	$(3.28\times10^{-28}\times7.24\times10^{18}\times P/T\times(T/300)^{-6.87}\times1.125$ $\times10^{-11}\times(T/300)^{-1.105})\times10^{(\log10(0.30)}/(1+(\log10(2.93$ $\times10^{-17}\times7.24\times10^{18}\times P/T\times(T/300)^{-5.765})/0.75-1.27$ $\times\log10(0.30))^2))/(2.926\times10^{-17}\times7.24\times10^{18}\times P/T$ $\times(T/300)^{-5.765})$ / molecules $^{-1}$ cm^3 s^{-1}	(R12)
NO$_2$+ OH → HNO$_3$	$3.2\times10^{-30}\times7.24\times10^{18}\times P/T\times(T/300)^{-4.5}\times3\times10^{-11}$ $\times10^{\log10(0.41)}/(1+(\log10(3.2\times10^{-30}\times7.24\times10^{18}\times P/T$	(R13)

$$\times (T/300)^{-4.5}/3\times 10^{-11})/(0.75\text{-}1.27$$
$$\times (\log 10(0.41))^2)/(3.2\times 10^{-30}\times 7.24\times 10^{18}\times P/T$$
$$\times (T/300)^{-4.5}+3\times 10^{-11}) \text{ / molecules}^{-1} \text{ cm}^3 \text{ s}^{-1}$$

$O_3 + OH \rightarrow HO_2$	$1.70\times 10^{-12}\times \exp(-940/T)$ / molecules^{-1} cm^3 s^{-1}	(R14)
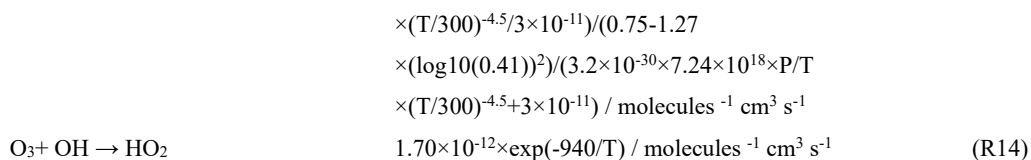
489   *The rate coefficient obtained from the MCM v3.3.1 model.

490   In total, three-stage simulations were carried out to obtain the 4-min photochemical reactions in

491   the reaction and reference chambers, and all three-stage models were operated in a time-dependent mode

492   with a 1 s resolution. In the 1st-stage, to establish a real atmospheric environment system, all observations

493   on 7 December 2021, 6:00-11:30, were used to constrain the model to obtain the mixing ratios of the

494   unmeasured species in the ambient atmosphere, including oxygenated VOCs (OVOCs, in total 16

495   species), non-methane hydrocarbons (in total 47 species), O_3, NO, NO_2, J values, T, RH, and pressure

496   (P). Because O_3-NO-NO_2 was not in a steady state when all species were constrained, we conducted a

497   2nd-stage simulation during 11:30–12:00. In this stage, we used the output mixing ratios of the

498   unmeasured species from the simulation in the last 1 s of the 1st-stage simulation as the input, which were

499   not constrained after providing initial values. For the measured species, O_3, NO, and NO_2 were no longer

500   constrained after providing initial values, while all other variables (including NO_X, VOCs, J values, RH,

501   T, P, etc.) were still constrained in a time-dependent mode with a 1 s resolution after providing initial

502   values. In the 3rd-stage, we modeled the 4-min photochemical reactions in the reaction and reference

503   chambers. We used the output mixing ratios of the unmeasured species (i.e., OH, HO_2, RO_2, SO_2, HONO,

504   etc.) from the simulation in the last 1 s of the 2nd-stage simulation and all measured values (i.e., O_3, NO,

505   NO_2, VOCs, J values, RH, T, P, etc.) as the model input, which were not constrained after providing

506   initial values. In addition, while maintaining the setup conditions for the 2nd-stage of the simulation, we

507   extended the simulation of the environment to 12:04 to obtain the modeled $P(O_3)_{net}$ in the environment

508   in the 3rd-stage simulation. The result is shown in orange marker in Fig. 10d. Figure 7 is an explicit

509   explanation of the 3rd-stage simulation in the reaction and reference chambers.
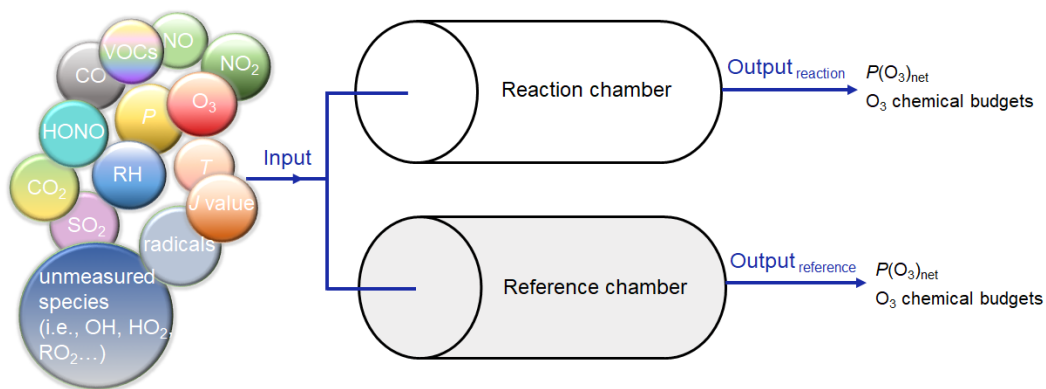
Figure 7: Explicit explanation of the 3rd-stage model simulation (input meteorological conditions: P: 1015.3 hPa, T: 295.6 K, RH: 39.7 %).

Specifically, because the photolysis frequencies play critical roles in the simulation of $P(O_3)_{net}$, the J values obtained from two methods (labeled method I and method II) were used in the 3rd-stage 4-min simulation. The J values used in method I were obtained from the measured values (including $J(NO_2)$, $J(O^1D)$, $J(HONO)$, $J(H_2O_2)$, $J(NO_3\_M)$, $J(NO_3\_R)$, $J(HCHO\_M)$, and $J(HCHO\_R)$) and the simulated values using the Tropospheric Ultraviolet and Visible (TUV) radiation model (version 5.3) (including $J(HNO_3)$, $J(CH_3CHO)$, $J(MACR)$, $J(MEK)$, $J(HOCH_2CHO)$, $J(C_2H_5CHO)$, $J(C_3H_7CHO)$, and $J(C_4H_9CHO)$).), while the J values in method II were all obtained from the simulated values using the TUV model, detailed information on these two methods is introduced in Appendix IV (Tables S12 and S13).

3.2.2 Radical chemistry in the reaction and reference chambers

The variations in the radical mixing ratios (i.e., HO_2, OH, RO_2) and NO_3, NO, NO_2, and O_3 mixing ratios obtained from method I and method II during the 3rd-stage 4-min model simulation are shown in Fig. 8 and Fig. S18, respectively. The production and destruction reactions of HO_2, OH, RO_2, and NO_3 in the reaction and reference chambers obtained from methods I and II are shown in Fig. 9 and Fig. S19, respectively, the production and destruction reactions of RO_X in the reaction and reference chambers obtained from methods I and II are shown in Fig. S20, the detailed ROx production pathways of NO_3+VOCs are shown in Fig. S21, and the final modeling results are shown in Fig. 10 and Fig. S22.

From Fig. 8, in the reaction chamber, the HO_2, OH, RO_2, and NO_3 concentrations first slightly increased and then became stable, and their final concentrations were 2.00×10^8, 7.64×10^6, 1.08×10^8, and 8.47×10^6 molecules cm^{-3}, respectively. In the reference chamber, the HO_2 and RO_2 concentrations dropped during the 1st half minute and rose afterward. The final HO_2 concentration (1.35×10^8 molecules cm^{-3}) was lower than that in the reaction chamber, while the RO_2 concentration exceeded that in the reaction chamber at the end of the 2nd minute and gradually became stable at 1.27×10^8 molecules cm^{-3}.

The OH concentration dropped significantly at the 1st minute and then became stable at approximately 6.16×10^5 molecules cm^{-3}. The NO_3 concentration rose significantly during the 4-min simulation and reached 3.55×10^7 molecules cm^{-3} at the end, which was much higher than that in the reaction chamber.
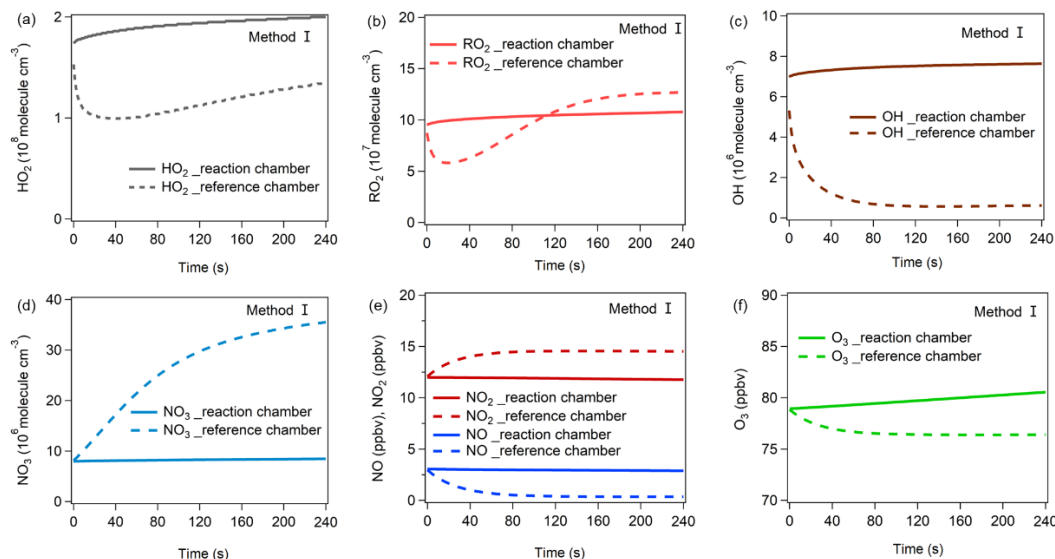
Figure 8: The variations of (a)HO_2, (b) RO_2, (c) OH, (d)NO_3, (e) NO, NO_2, and (f) O_3 mixing ratios during the 3rd-stage 4-min model simulation using method I. The mixing ratios changes of these items for method II is shown in Fig. S18.

OH, HO_2, RO_2, and NO_3 concentrations greatly impact the O_3 production and destruction rate. To better understand the factors that drive the OH, HO_2, RO_2, and NO_3 concentration changes, we have added their production and destruction pathways in Fig. 9. We found that the decrease in HO_2 and RO_2 concentrations in the reference chamber in the 1st half minute was mainly due to NO titration effects, as high NO mixing ratios existed during the 1st half minute. The increase in HO_2 concentrations afterward was largely attributable to $RO+O_2$ reaction/RO decomposition, OH+CO/VOCs reaction, OVOCs photolysis (i.e., $C_3H_4O_2$, $C_2H_2O_2$, $C_4H_6O_2$), and NO_3+VOCs reaction, and the increase in RO_2 concentrations afterward were largely attributable to OH+VOCs oxidation, OVOCs photolysis and O_3+VOCs reaction. The main OH sources in the reference chamber were both HO_2+NO in method I and method II. Due to sufficiently high $J(NO_3)$ (~ 90% of that in the reaction chamber) and NO_2 concentrations in the reference chamber, the NO_3 photolysis and NO_2+NO_3 reaction consumed NO_3 in the reference chamber, but the NO_3 concentrations were still sufficiently high due to high production rates of NO_3 at the same time. The main NO_3 source in the reference chamber was the NO_2+O_3 reaction, followed by N_2O_5 decomposition. The NO concentrations were relatively high in the 1st minute and

556 consumed NO_3 very quickly, but due to continuous NO_3 sources, the net NO_3 production rates ($P(NO_3)_{net}$)

557 were positive (as shown in Fig. 9), which caused the NO_3 concentration to continue to increase (as shown

558 in Fig. 8d). The main difference in NO_3 production in the reference chamber compared to that in the

559 reaction chamber was the much higher N_2O_5 decomposition, which was mainly due to the high NO_2

560 concentrations in the reference chamber. On the other hand, although the $NO+NO_3$ reaction was also one

561 of the dominant NO_3 destruction pathways, NO_3 consumed by the $NO+NO_3$ reaction was significantly

562 smaller than NO_3 produced by the NO_2+O_3 reaction. Furthermore, in order to check if the NO_3+VOCs

563 reactions exists, we extracted all the $P(ROx)$ pathways related to NO_3+VOCs reactions during the 3rd-

564 stage 4-min model simulation in the reaction and reference chambers in method I, as shown in Fig. S20.

565 We found that the NO_3+VOCs reactions are mostly related to the OVOCs (i.e. 6-Ethyl-m-cresol and 3-

566 Ethyl-6-methylbenzene-1,2-diol) in Fig. S21. The production and destruction rates of ROx are shown in

567 Fig. S20.

568
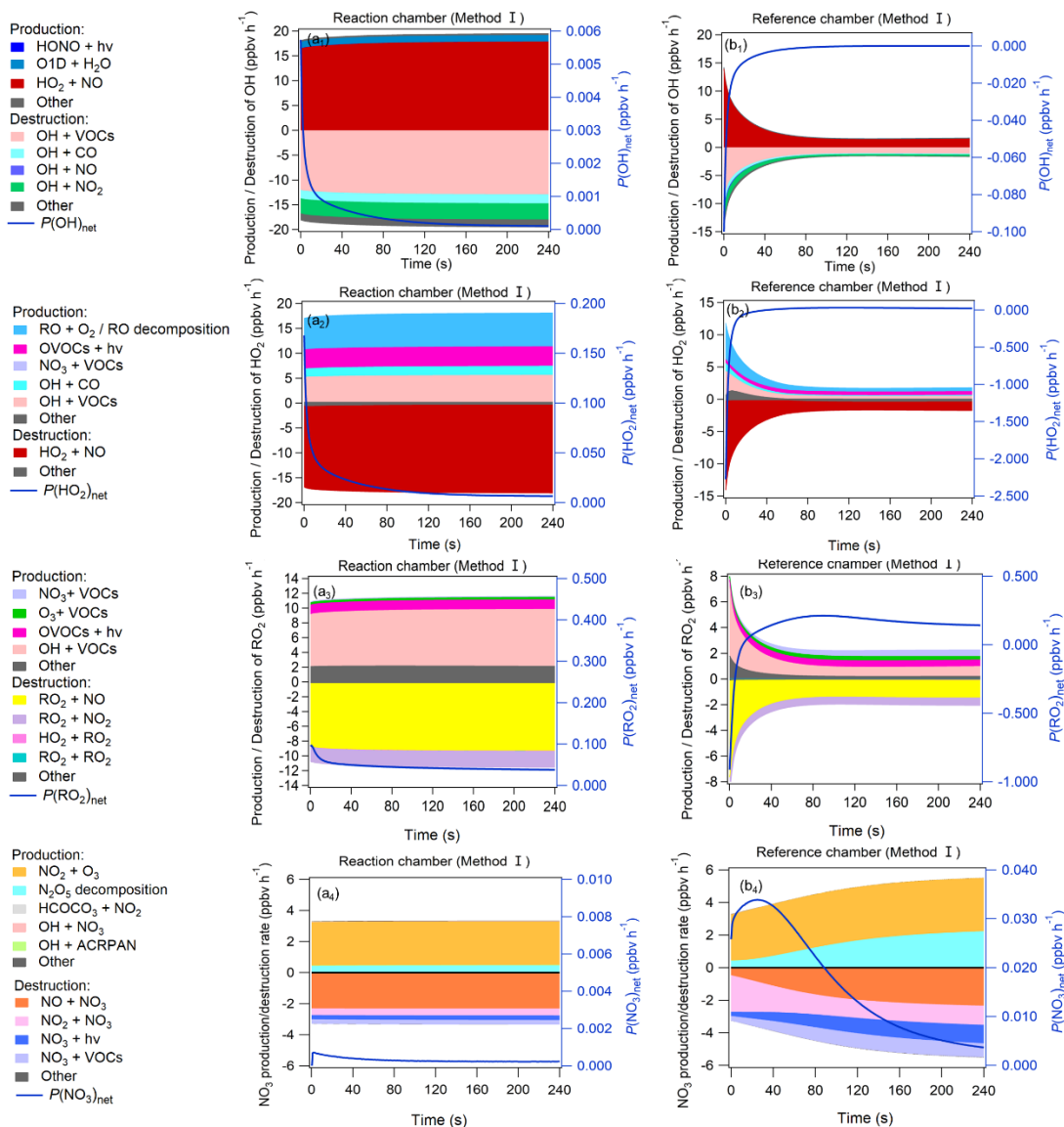
Figure 9: Production and destruction pathways of OH (a_1-b_1), HO$_2$ (a_2-b_2), RO$_2$ (a_3-b_3), and NO$_3$ (a_4-b_4) during the 3rd-stage 4-min model simulation in the reaction and reference chambers in method I. The related contents for method II (c)-(d) are shown in Fig. S19 in the supplementary materials.

3.2.3 $P(O_3)_{net}$ formation and destruction pathways in the reaction and reference chambers

Figures 10a–d show the modeled $P(O_3)_{net}$ and the sources and sinks of various species during the 3rd-stage 4-min simulation. Figure 10a shows the steady state of $P(O_3)_{net}$ and the various species in the ambient atmosphere achieved in the last 1 s of the 2nd-stage simulation; Figures 10b and c show the modeled $P(O_3)_{net}$ and the O$_3$ chemical budgets in the reaction and reference chambers during the model simulation period; Figure 10d summarizes the modeled $P(O_3)_{net}$ in the ambient air (represented as blue and orange markers at the time when the ambient air was going in and out of the NPOPR system, respectively) and the modeled $P(O_3)_{net}$ in the reaction and reference chambers. To compare the modeled results with our measured results, we calculated the integral mean of the modeled $P(O_3)_{net}$ in the reaction

582   and reference chambers and appended the related measured $P(O_3)_{net}$ value during the 4-min simulation

583   time onto Fig. 10d (green maker). Furthermore, the reaction weights of different production and

584   destruction reaction processes of O_3 are shown in Figs. 10e–h.
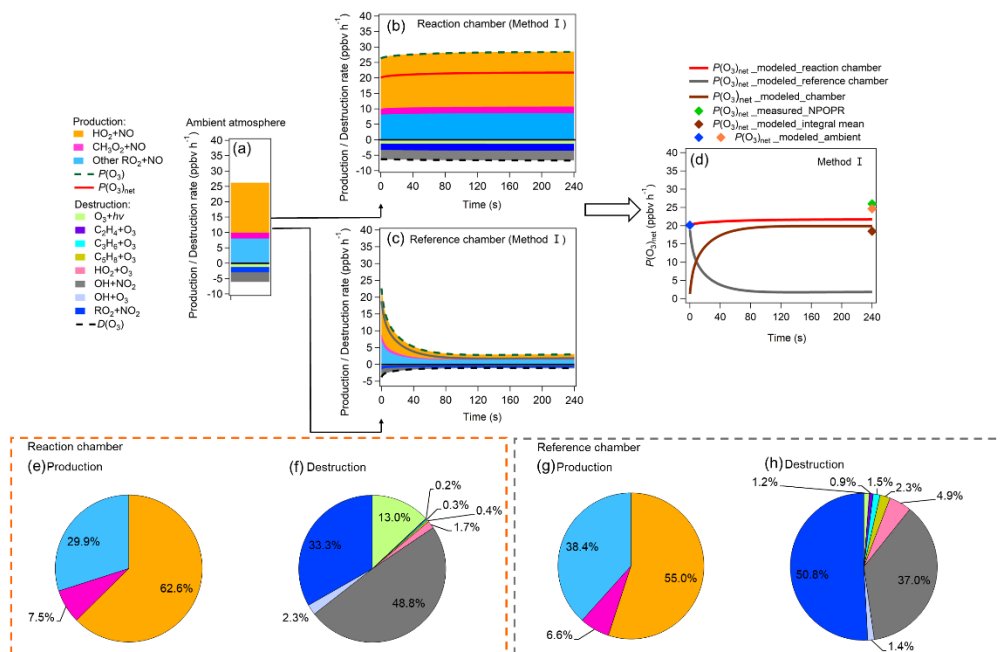
585

586   **Figure 10: (a)–(c) show the modeled $P(O_3)_{net}$ and the O_3 chemical budgets in (a) the ambient atmosphere when**

587   **injected into the reaction and reference chambers and (b–c) the reaction and reference chambers during the**

588   **4-min model simulation; (d) shows $P(O_3)_{net}$, where $P(O_3)_{net\_modeled\_ambient}$ represent the modeled $P(O_3)_{net}$**

589   **in the ambient air at the time before (blue marker) and after (orange marker) the sampled ambient air was**

590   **injected into the dual-channel reaction chamber. $P(O_3)_{net\_modeled\_reaction}$ chamber and**

591   **$P(O_3)_{net\_modeled\_reference}$ chamber represent the $P(O_3)_{net}$ changing trend during the 4-min photochemical**

592   **reactions in the reaction and reference chambers, respectively, $P(O_3)_{net\_modeled\_chamber}$ =**

593   **$P(O_3)_{net\_modeled\_reaction}$ chamber–$P(O_3)_{net\_modeled\_reference}$ chamber, $P(O_3)_{net\_modeled\_integral}$ mean**

594   **represents the integral mean of the $P(O_3)_{net\_modeled\_chamber}$, and $P(O_3)_{net\_measured\_NPOPR}$ represent**

595   **the measured $P(O_3)_{net}$ by NPOPR detection system. (e)–(h) show the reaction weights of each production and**

596   **destruction reactions process of O_3 in the reaction and reference chambers in method I.**

597   Figure 10a-h shows the contribution of different reaction pathways to $P(O_3)$ and $D(O_3)$. $P(O_3)$ and

598    $D(O_3)$ were almost the same within the 4-min reaction in the reaction chamber (all species reached a

599   steady-state condition), while $P(O_3)$ and $D(O_3)$ in the reference chamber decreased significantly within

600   the 1st min and remained stable in the following minutes. In the reaction chamber, the HO_2+NO reaction

601   contributed most to $P(O_3)$, accounting for 62.6 % of the total $P(O_3)$, with an integral mean value of 17.5

602   ppbv h^{-1} in the reaction chamber. The second important pathway of $P(O_3)$ was RO_2+NO (accounting for

603   37.4 % of the total $P(O_3)$). The reaction of RO_2+NO core presents more than approximately 1200 types

604   of RO_2 radicals, and the pathway of CH_3O_2+NO contributed 7.5 % of the total $P(O_3)$. The most important

contributor of $D(O_3)$ was OH+NO$_2$ (48.8 %), followed by RO$_2$+NO$_2$ (33.3 %), O$_3$ photolysis (13.0 %),

O$_3$+OH (2.3 %), O$_3$+HO$_2$ (1.7 %), C$_5$H$_8$+O$_3$ (0.4 %), C$_3$H$_6$+O$_3$ (0.3 %), and C$_2$H$_4$+O$_3$ (0.2 %). In the

reference chamber, the integral mean value of the HO$_2$+NO reaction was 2.3 ppbv h^{-1}, which had the

largest contribution to $P(O_3)$ (accounting for 55.0 %). The second largest contributor of $P(O_3)$ was

RO$_2$+NO (accounting for 45.0 % of the total $P(O_3)$), in which the pathway of CH$_3$O$_2$+NO contributed

6.6 % of the total $P(O_3)$. The most important contributor of $D(O_3)$ was RO$_2$+NO$_2$ (50.8 %), followed by

OH+NO$_2$ (37.0 %), O$_3$+HO$_2$ (4.9 %), C$_5$H$_8$+O$_3$ (2.3 %), C$_3$H$_6$+O$_3$ (1.5 %), O$_3$+OH (1.4 %), O$_3$ photolysis

(1.2 %), and C$_2$H$_4$+O$_3$ (0.9 %). For all $P(O_3)$ reactions, the weight of the RO$_2$+NO reaction in the

reference chamber was 7.5 % higher than that in the reaction chamber; however, for all $D(O_3)$ reactions,

the weight of the RO$_2$+NO$_2$ reaction in the reference chamber was 17.5 % higher than that in the reaction

chamber, which mitigates the high $P(O_3)$ caused by RO$_2$+NO in the reference chamber. Furthermore, the

weight of the OH+NO$_2$ reaction in the reference chamber was 11.9 % lower than that in the reaction

chamber, which may be the main reason that led to NO$_2$ mixing ratios in the reference chamber being

much higher than those in the reaction chamber. It is worth noting that the different reaction pathways of

$P(O_3)$ and $D(O_3)$ stabilized at approximately 1.5 min for both methods I and II (as shown in Figs. 10 and

S22), and the radicals that play critical roles in photochemical O$_3$ formation, such as HO$_2$, RO$_2$ and OH,

reached quasi-steady states in approximately 3 min (as shown in Figs. 8 and S18). As the lowest

experimental residence time in the reaction and reference chambers was 3.8 min at an air flow rate of 5

L min^{-1}, the photochemical reaction time at different air flow rates in the NPOPR system is sufficient for

investigating $P(O_3)_{net}$, and it is reasonable for us to set the alternate ambient air sampling time for the

reaction and reference chambers at 2 min, where the ambient air actually has already reacted for at least

3.8 min in the chambers.

The $P(O_3)_{net}$ value measured by the NPOPR detection system at 12:04 was 26.0 ppbv h^{-1}, which

was 1.4 ppbv h^{-1} higher than the modeled $P(O_3)_{net}$ value in the ambient air (orange marker in Fig. 10d,

24.6 ppbv h^{-1}) and 7.5 ppbv h^{-1} higher than the modeled $P(O_3)_{net}$ value of the NPOPR system (brown

marker in Fig. 10d, 18.5 ppbv h^{-1}, calculated from the integral mean of the 3rd-stage 4-min modeled

$P(O_3)_{net}$ in the reaction and reference chambers). Here, we note that for a better comparison between the

measured and modeled $P(O_3)_{net}$ values, the measured $P(O_3)_{net}$ used here was obtained from a 4-min time

resolution, which is 1.4 ppbv h^{-1} higher than the measured $P(O_3)_{net}$ value used in Fig. 6 (1-h time

resolution). The ratio of measured and modeled $P(O_3)_{net}$ values was 1.4, which is consistent with the measured-to-modeled ratio of the cumulative $P(O_3)_{net}$ (1.3 and 1.4) obtained from previous studies (Cazorla et al., 2012; Ren et al., 2013), where $P(O_3)_{net}$ values were also measured directly in the atmosphere and were independent of the OH and HO_2 measurements. The reason for the difference between the measured and modeled $P(O_3)_{net}$ here may be due to the inaccurate estimation of HO_2/RO_2 radicals; for example, Ren et al. (2013) found that $P(O_3)$ calculated from the modeled HO_2 was lower than that calculated from the measured HO_2. The unknown HO_2 source should be identified for a more accurate estimation of $P(O_3)_{net}$ in future studies.

Additionally, the modeled $P(O_3)_{net}$ using the J values obtained from method II was 9.3 ppbv h^{-1} lower than the measured $P(O_3)_{net}$, and this discrepancy was slightly larger than that using method I, as shown in Appendix IV (Fig. S22). The differences in the measured and modeled $P(O_3)_{net}$ by method I and method II were 28.8 % and 35.8 %, respectively. This difference was mainly due to the transmittance of $J(NO_2)$ in method II (30 %) being much higher than that in method I (9 %), and NO_2 photolysis products were involved in the main reaction of O_3 production of HO_2+NO and RO_2+NO, so the modeled $P(O_3)_{net}$ in the reference chamber was slightly overestimated in method II, thus leading to an underestimation of the final $P(O_3)_{net}$.

In conclusion, modeling tests demonstrated that the radicals and gas species in the reaction chamber of the NPOPR detection system were similar to those in genuine ambient air, while these radicals also unexpectedly existed in the reference chamber. This was mainly because the UV protection film used by the reference chamber did not completely filter out sunlight, which led to the low transmittance of light ranging from 390 nm to 790 nm. The $P(O_3)_{net}$ biases caused by this interference modeled in method I and method II were 13.9 % and 22.3 %, respectively, which ensured that the measured $P(O_3)_{net}$ by the NPOPR detection system should be regarded as the lower limit values of real $P(O_3)_{net}$ in the atmosphere. We recommend that the J values obtained from method I should be used in the model simulation, which can better explain the photochemical formation of O_3 in the actual atmosphere, but if direct J value measurements cannot be achieved during field observations, the J values obtained from method II would also be acceptable in modeling studies.

Furthermore, because the NO_2 data used here were measured by a commercially available chemiluminescence NOx monitor, the NO_2 and NOx mixing ratios would be overestimated due to NOz

663 interference (i.e., HNO_3, PANs, HONO, etc.) (Dunlea et al., 2007). According to our test, the

664 chemiluminescence technique could bias NO_2 by 5 % compared to the CAPS technique, which is

665 regarded as a trustworthy NO_2 measurement technique without chemical interference. Therefore, we

666 simulated the interference of NO_2 measured by a chemiluminescence NOx monitor in method I as follows:

667 reducing and increasing the ambient NO_2 mixing ratios by 5 % in the 3rd-stage 4-min simulation in the

668 reaction and reference chambers. The results show that increasing and decreasing NO_2 by 5 % resulted

669 in a decrease in $P(O_3)_{net}$ by 1.64 % and 3.68 %, respectively (as shown in Fig. S23), which is much

670 smaller than the bias caused by $P(O_3)_{net}$ in the reference chambers (which were 13.9 % and 22.3 % for

671 method I and method II, respectively).

672 **4 Conclusions**

673 We modified and improved a net photochemical ozone production rate (NPOPR) detection system based

674 on a dual-channel reaction chamber technique, which provides more accurate results and has broader

675 application potential compared to previous studies. The main improvements of NPOPR detection system

676 compared to previous studies were as follows: (1) improved the design of the reaction and reference

677 chambers to make sure they have good airtightness; (2) changed the air sampling structure to enable the

678 total air flow rates change freely from 1.3 to 5 L min^{-1} in the reaction and reference chambers, which can

679 make the NPOPR system achieve different limits of detection (LODs) and appliable to different ambient

680 environment; (3) characterized the NPOPR detection system at different air flow rates to optimize the

681 $P(O_3)_{net}$ measurements, the LODs of the NPOPR detection system are 0.07, 1.4, and 2.3 ppbv h^{-1} at air

682 flow rates of 1.3, 3, and 5 L min^{-1}, respectively; (4) tested the performance of both reaction and reference

683 chambers by combining the field measurement and the MCM modelling method.

684 The NPOPR detection system was employed in the field observation at the Shenzhen

685 Meteorological Gradient Tower (SZMGT), which is located in PRD, China. During the measurement

686 period, the $P(O_3)_{net}$ was around zero during nighttime and ranged from ~ 0 to 34.1±7.8 ppbv h^{-1} during

687 daytime (from 6:00–18:00), with the average value of 12.8 (±5.5) ppbv h^{-1}. Besides, $P(O_3)_{net}$ start to

688 increase at around 7:00 at local time, this may be due to the rise of the O_3 precursors (i.e., VOCs)

689 transported down from the high-altitude atmospheric residual layer to the near-surface and the increase

690 of solar radiation intensity increased the atmospheric oxidation capacity. $P(O_3)_{net}$ was then reaches a peak

691   at around 12:00 at noon time, by coupling with diurnal O_3 mixing ratios trends, we confirmed that the

692   ground-level O_3 mixing ratios were influenced by both photochemical production and physical transport.

693   In order to clarify the detailed photochemical reaction processes in the reaction and reference

694   chambers of NPOPR system, we modeled the $P(O_3)_{net}$ on 7 December 2021, 12:00-12:04 in the reaction

695   and reference chambers using MCM v3.3.1. As the photolysis frequencies of different species (J values)

696   play critical roles in the formation of $P(O_3)_{net}$, the J values obtained from two methods were used in the

697   4-min chamber photochemical reaction (labeled as method I and method II), in method I , eight main J

698   values (e.g., $J(NO_2)$, $J(O^1D)$, $J(HONO)$, etc.) were measured directly, and other J values were obtained

699   from the simulated values using the Tropospheric Ultraviolet and Visible (TUV) radiation model, while

700   in method II, J values were all obtained from the simulated values using TUV model (as described in

701   Sect. 3.2). Modeling tests demonstrated that the mixing ratios of different radicals and gas species (i.e.,

702   OH, HO_2, RO_2, NO_3, NO, NO_2, and O_3) in the reaction chamber were similar with those in the real

703   ambient environment, while due to the UV protection film used by the reference chamber does not

704   completely filter out the sunlight, there was low transmittance of the light ranged from 390 nm to 790

705   nm. In the reaction chamber, the contribution of different reactions to $P(O_3)$ and $D(O_3)$ modeled

706   method I and II were quite similar, where the HO_2+NO reaction contributed most to $P(O_3)$ (~ 62.6 %),

707   followed by the RO_2+NO reaction (~ 37.4 %). The OH+NO_2 reaction contributed most to $D(O_3)$, which

708   accounted for ~ 48.9 %, followed by the RO_2+NO_2 reaction O_3 photolysis, which accounted for ~ 33.3 %

709   and 13.0 %, respectively. In the reference chamber, the contribution of different reactions to $P(O_3)$ and

710    $D(O_3)$ modeled by method I and II were different, where the HO_2+NO reaction contributed ~ 55.0 % and

711   ~ 58.2 % to the total $P(O_3)$, respectively, and RO_2+NO contributed ~ 44.9 % and 41.8 % to the total

712    $P(O_3)$, respectively. The most important contributor of $D(O_3)$ modeled by method I was RO_2+NO_2

713   (50.8 %), followed by OH+NO_2 (37.0 %), while the most important contributor of $D(O_3)$ modeled by

714   method II was OH+NO_2 (46.8 %), followed by RO_2+NO_2 (44.1 %). For all $P(O_3)$ reactions, the weight

715   of RO_2+NO reaction in the reference chamber was 7.5 % and 4.3 % higher than that in the reaction

716   chamber in method I and II, respectively, however, for all $D(O_3)$ reactions, the weight of RO_2+NO_2

717   reaction in the reference chamber was 17.5 % and 10.9 % higher than that in the reaction chamber in

718   method I and II, respectively, which will somehow mitigate the high $P(O_3)$ caused by RO_2+NO in the

719   reference chamber. The different reaction pathways of $P(O_3)$ and $D(O_3)$ had stabilized at around 1.5 min,

720 and the radicals that play critical roles in photochemical O_3 formation, such as HO_2, RO_2 and OH, reached

721 quasi-steady states in about 3 min, the long enough ambient air residence time in the reaction and

722 reference chambers ($\geq$ 3.8 min) make the photochemical reaction time at different air flow rates in the

723 NPOPR system sufficient enough for investigating the $P(O_3)_{net}$, and it is reasonable for us to set the

724 alternate ambient air sampling time for the reaction and reference chambers at 2 min, where the ambient

725 air actually has already reacted for at least 3.8 min in the chambers.

726   The biases of the modeled $P(O_3)_{net}$ caused by the interference of the reactions in the reference

727 chamber in method I and method II were 13.9 % and 22.3 %, respectively; thus, the measured $P(O_3)_{net}$

728 by the NPOPR detection system should be regarded as the lower limit values of the real $P(O_3)_{net}$ in the

729 atmosphere. Nevertheless, the measured $P(O_3)_{net}$ values were 7.5 and 9.3 ppbv h^{-1} higher than the

730 modeled $P(O_3)_{net}$ values obtained from methods I and II, respectively, which may be due to the inaccurate

731 modeling of HO_2/RO_2 radicals. Short-lived intermediate measurements coupled with direct $P(O_3)_{net}$

732 measurements are needed in future study in order to studies to better understand the photochemical

733 production and destruction mechanisms of O_3. We recommend that the J values obtained from method I

734 should be used in the model simulation, which can better explain the photochemical formation of O_3 in

735 the actual atmosphere, but if direct J value measurements cannot be achieved during field observations,

736 the J values obtained from method II would also be acceptable in modeling studies.

737   The self-built NPOPR detection system in this study filled the gap in the observation method in

738 China. The research results not only help us to understand the tropospheric O_3 budget but also provide

739 an important data basis for formulating correct O_3 pollution prevention measures and control strategies.

740

741 *Data availability.* The observational data used in this study are available from corresponding authors

742 upon request (junzhou@jnu.edu.cn).

743 *Author contributions.* JZ, BY, and MS designed the experiment, YXH and JZ developed and assembled

744 the NPOPR detection system, YXH, JZ, JPZ, BY, YW, YFW, SCY, YWP, JPQ, XJH, XS and YBC

745 collected and analyzed the data YXH and JZ wrote the manuscript, all authors revised the manuscript.

746 *Competing interests.* The authors declare that they have no known competing interests.

747 *Acknowledgements.* This study was funded by the Key-Area Research and Development Program of

748 Guangdong Province (grant no. 2020B1111360003), and the Natural Science Foundation of Guangdong

749   Province (grant no. 2020A1515110526). We thank Nan Ma and Xiaofeng Su for the HONO production

750   experiment.

751   **References**

752   Avnery, S., Mauzerall, D. L., Liu, J., and Horowitz, L. W.: Global crop yield reductions due to surface

753   ozone exposure: 1. Year 2000 crop production losses and economic damage, Atmos. Environ., 45,

754   2284-2296, https://doi.org/10.1016/j.atmosenv.2010.11.045, 2011.

755   Baier, B. C., Brune, W. H., Lefer, B. L., Miller, D. O., and Martins, D. K.: Direct ozone production rate

756   measurements and their use in assessing ozone source and receptor regions for Houston in 2013, Atmos.

757   Environ., 114, 83-91, http://dx.doi.org/10.1016/j.atmosenv.2015.05.033, 2015.

758   Baier B C, Brune W H, Miller D O, et al., Higher measured than modeled ozone production at increased

759   NOx levels in the Colorado Front Range, Atmos. Chem. Phys., 17: 11273–11292,

760   https://doi.org/10.5194/acp-17-11273-2017, 2017.

761   Bell, M. L., McDermott, A., Zeger, S. L., Samet, J. M., and Dominici, F.: Ozone and short-term mortality

762   in 95 US urban communities, J. Am. Med. Assoc. 1987-2000., 292, 2372-

763   2378, https://doi.org/10.1001/jama.292.19.2372, 2004.

764   Berman, J. D., Fann, N., Hollingsworth, J. W., Pinkerton, K. E., Rom, W. N., Szema, A. M., Breysse, P.

765   N., White, R. H., and Curriero, F. C.: Health benefits from large-scale ozone reduction in the United

766   States, Environ. Health. Persp., 120, 1404-10, https://doi.org/10.1289/ehp.1104851, 2012.

767   Cazorla, M., Brune, and W. H.: Measurement of ozone production sensor, Atmos. Meas. Tech., 3, 545-

768   555, https://doi.org/10.5194/amt-3-545-2010, 2010.

769   Cazorla, M., Brune, W. H., Ren, X., and Lefer, B.: Direct measurement of ozone production rates in

770   Houston in 2009 and comparison with two estimation methods, Atmos. Chem. Phys., 12, 1203-1212,

771   https://doi.org/10.5194/acp-12-1203-2012, 2012.

772   Dunlea, E. J., Herndon, S. C., Nelson, D. D., Volkamer, R. M., Martini, F. S., Sheehy, P. M., Zahniser,

773   M. S., Shorter, H., Wormhoudt, J. C., Lamb, B. K., Allwine, E. J., Gaffney, J. S., Marley, N. A., Grutter,

774   M., Marquez, C., Blanco, S., Cardenas, B., Retama, A., Villegas, C. R. R., Kolb, C. E., Molina, L. T.,

775   and Molina, M. J.: Evaluation of nitrogen dioxide chemiluminescence monitors in a polluted urban

776   environment, Atmos. Chem. Phys., 7, 2691–2704, https://doi.org/10.5194/acp-7-2691-2007, 2007.

777   Jenkin, M. E., Young, J. C., and Rickard, A. R.: The MCM v3.3.1 degradation scheme for isoprene,

778   Atmos. Chem. Phys., 15, 11433-11459, https://doi.org/10.5194/acp-15-11433-2015, 2015.

779 Kanaya, Y., Tanimoto, H., Yokouchi, Y., Fumikazu Taketani, F. T., Komazaki, Y., Irie, H., Takashima, H.,

780 Pan, X., Nozoe, S., and Inomata, S.: Diagnosis of photochemical ozone production rates and limiting

781 factors in continental outflow air masses reaching Fukue Island, Japan: ozone-control implications,

782 Aerosol. Air. Qual. Res., 16, 430-441, https://doi.org/10.4209/aaqr.2015.04.0220, 2016.

783 Karakatsani, A., Kapitsimadis, F., Pipikou, M., Chalbot, M. C., Kavouras, I. G., Orphanidou, D., Papiris,

784 S., and Katsouyanni, K.: Ambient air pollution and respiratory health effects in mail carriers, Environ.

785 Res., 110, 278-85, https://doi.org/10.1016/j.envres.2009.11.002, 2010.

786 Lee, S.-B., Bae, G.-N., Lee, Y.-M., Moon, K.-C., and Choi, M.: Correlation between light intensity and

787 ozone formation for photochemical smog in urban air of seoul, Aerosol. Air. Qual. Res., 10, 540-549,

788 https://doi.org/10.4209/aaqr.2010.05.0036, 2010.

789 Liu, S. C.: Possible effects on froposcheric O3 and OH due to NO emissions, Geophys. Res. Lett., 4,

790 325-328, https://doi.org/10.1029/GL004i008p00325, 1977.

791 Liu, X., Wang, N., Lyu, X., Zeren, Y., Jiang, F., Wang, X., Zou, S., Ling, Z., and Guo, H.: Photochemistry

792 of ozone pollution in autumn in Pearl River Estuary, South China, Sci. Total Environ., 754, 141812,

793 https://doi.org/10.1016/j.scitotenv.2020.141812, 2020.

794 Luecken, D. J., Phillips, S., Sarwar, and G., Jang, C.: Effects of using the CB05 vs. SAPRC99 vs. CB4

795 chemical mechanism on model predictions: Ozone and gas-phase photochemical precursor

796 concentrations, Atmos. Environ., 42, 5805-5820, https://doi.org/10.1016/j.atmosenv.2007.08.056,

797 2008.

798 Lu, K., Zhang, Y., Su, H., Brauers, T., Chou, C. C., Hofzumahaus, A., Liu, S. C., Kita, K., Kondo, Y,

799 Shao, M., Wahner, A., Wang, J., Wang, X., and Zhu, T.: Oxidant (O3+ NO2) production processes and

800 formation regimes in Beijing, J. Geophys. Res. Atmos., 115, D07303,

801 https://doi.org/10.1029/2009JD012714, 2010.

802 Malley, C. S., Henze, D. K., Kuylenstierna, J. C. I., Vallack, H. W., Davila, Y., Anenberg, S. C., Turner,

803 M. C., and Ashmore, M. R.: Updated global estimates of respiratory mortality in adults ≥30 years of

804 age attributable to long-term ozone exposure, Environ. Health. Persp., 125, 087021,

805 https://doi.org/10.1289/EHP1390, 2017.

806 Martinez, M.: OH and HO2 concentrations, sources, and loss rates during the Southern Oxidants Study

807 in Nashville, Tennessee, summer 1999, J. Geophys. Res.-Atmos., 108, 4617,

808 https://doi.org/10.1029/2003JD003551, 2003.

809 Mazzuca, G. M.,Ren, X., Loughner, C. P., Estes, M., Crawford, J. H., Pickering, K. E., Weinheimer, A.

810 J., and Dickerson, R. R.: Ozone production and its sensitivity to NOx and VOCs: results from the

811 DISCOVER-AQ field experiment, Houston 2013, Atmos. Chem. Phys., 16, 14463-14474,

812 https://doi.org/10.5194/acp-16-14463-2016, 2016.

813 Mills, G., Sharps, K., Simpson, D., Pleijel, H., Broberg, M., Uddling, J., Jaramillo, F., Davies, W. J.,

814 Dentener, F., Van den Berg, M., Agrawal, M., Agrawal, S. B., Ainsworth, E. A., Buker, P., Emberson,

815 L., Feng, Z., Harmens, H., Hayes, F., Kobayashi, K., Paoletti, E., and Van Dingenen, R.: Ozone

816 pollution will compromise efforts to increase global wheat production, Glob. Chang. Biol., 24, 3560-

817 3574, https://doi.org/10.1111/gcb.14157, 2018.

818 O'Neill, M. S., Jerrett, M., Kawachi, I., Levy, J. I., Cohen, A. J., Gouveia, N., Wilkinson, P., Fletcher, T.,

819 Cifuentes, L., Schwartz, J.: Health, wealth, and air pollution: advancing theory and methods, Environ.

820 Health. Persp., 111, 1861-70, https://doi.org/10.1289/ehp.6334, 2003.

821 Pan, X.; Kanaya, Y., Tanimoto, H., Inomata, S., Wang, Z., Kudo, S., and Uno, I.: Examining the major

822 contributors of ozone pollution in a rural area of the Yangtze River Delta region during harvest season,

823 Atmos. Chem. Phys., 15, 6101-6111, https://doi.org/10.5194/acp-15-6101-2015, 2015.

824 Ren, X., van Duin, D., Cazorla, M., Chen, S., Mao, J., Zhang, L., Brune, W. H., Flynn, J. H., Grossberg,

825 N., Lefer, B. L., Rappenglück, B., Wong, K. W., Tsai, C., Stutz, J., Dibb, J. E., Thomas Jobson, B.,

826 Luke, W. T., and Kelley, P.: Atmospheric oxidation chemistry and ozone production: results from

827 SHARP 2009 in Houston, Texas, J. Geophys. Res.-Atmos., 118, 5770-5780,

828 https://doi.org/10.1002/jgrd.50342, 2013.

829 Sadanaga, Y., Kawasaki, S., Tanaka, Y., Kajii, Y., and Bandow, H.: New system for measuring the

830 photochemical ozone production rate in the atmosphere, Environ. Sci. Technol., 51, 2871-2878,

831 https://doi.org/10.1021/acs.est.6b04639, 2017.

832 Shen, H., Liu, Y., Zhao, M., Li, J., Zhang, Y., Yang, J., Jiang, Y., Chen, T., Chen, M., Huang, X., Li, C.,

833 Guo, D., Sun, X., Xue, L., and Wang, W.: Significance of carbonyl compounds to photochemical ozone

834 formation in a coastal city (Shantou) in eastern China, Sci. Total. Environ., 764, 144031,

835 https://doi.org/10.1016/j.scitotenv.2020.144031, 2021.

836 Sklaveniti, S., Locoge, N., Stevens, P. S., Wood, E., Kundu, S., and Dusanter, S.: Development of an

instrument for direct ozone production rate measurements: measurement reliability and current limitations, Atmos. Meas. Tech., 11, 741-761, https://doi.org/10.5194/amt-11-741-2018, 2018.

Tadic, I., Crowley, J. N., Dienhart, D., Eger, P., Harder, H., Hottmann, B., Martinez, M., Parchatka, U., Paris, J.-D., Pozzer, A., Rohloff, R., Schuladen, J., Shenolikar, J., Tauer, S., Lelieveld, J., and Fischer, H.: Net ozone production and its relationship to nitrogen oxides and volatile organic compounds in the marine boundary layer around the Arabian Peninsula, Atmos. Chem. Phys., 20, 6769-6787, https://doi.org/10.5194/acp-20-6769-2020, 2020.

Wang, C., Yuan, B., Wu, C., Wang, S., Qi, J., Wang, B., Wang, Z., Hu, W., Chen, W., Ye, C., Wang, W., Sun, Y., Wang, C., Huang, S., Song, W., Wang, X., Yang, S., Zhang, S., Xu, W., Ma, N., Zhang, Z., Jiang, B., Su, H., Cheng, Y., Wang, X., and Shao, M.: Measurements of higher alkanes using NO+ chemical ionization in PTR-ToF-MS: important contributions of higher alkanes to secondary organic aerosols in China, Atmos. Chem. Phys., 20, 14123–14138, https://doi.org/10.5194/acp-20-14123-2020, 2020a.

Wang, F., An, J., Li, Y., Tang, Y., Lin, J., Qu, Y., Chen, Y., Zhang, B., and Zhai, J.: Impacts of uncertainty in AVOC emissions on the summer ROx budget and ozone production rate in the three most rapidly-developing economic growth regions of China, Adv. Atmos. Sci., 31, 1331-1342, https://doi.org/10.1007/s00376-014-3251-z, 2014.

Wolfe, G. M., Marvin, M. R., Roberts, S. J., Travis, K. R., and Liao, J.: The Framework for 0-D Atmospheric Modeling (F0AM) v3.1, Geosci. Model. Dev., 9, 3309-3319, https://doi.org/10.5194/gmd-9-3309-2016, 2016.

Wu, C., Wang, C., Wang, S., Wang, W., Yuan, B., Qi, J., Wang, B., Wang, H., Wang, C., Song, W., Wang, X., Hu, W., Lou, S., Ye, C., Peng, Y., Wang, Z., Huangfu, Y., Xie, Y., Zhu, M., Zheng, J., Wang, X., Jiang, B., Zhang, Z., and Shao, M.: Measurement report: Important contributions of oxygenated compounds to emissions and chemistry of volatile organic compounds in urban air, Atmos. Chem. Phys., 20, 14769–14785, https://doi.org/10.5194/acp-20-14769-2020, 2020.

Yuan, B., Chen, W., Shao, M., Wang, M., Lu, S., Wang, B., Liu, Y., Chang, C.-C., and Wang, B.: Measurements of ambient hydrocarbons and carbonyls in the Pearl River Delta (PRD), China, Atmos. Res., 116, 93-104, https://doi.org/10.1016/j.atmosres.2012.03.006, 2012.

Zhang, A., Lin, J., Chen, W., Lin, M., and Lei, C.: Spatial-temporal distribution variation of ground-level

866   ozone in China's Pearl River Delta metropolitan region, Int. J. Environ. Res. Public Health., 18, 872,

867   https://doi.org/10.3390/ijerph 18030872, 2021.

868 Zhou, W., Cohan, D. S., and Henderson, B. H.: Slower ozone production in Houston, Texas following

869   emission reductions: evidence from Texas Air Quality Studies in 2000 and 2006, Atmos. Chem. Phys.,

870   14, 2777-2788, https://doi.org/10.5194/acp-14-2777-2014, 2014.

871 Zhu, M., Dong, H., Yu, F., Liao, S., Xie, Y., Liu, J., Sha, Q., Zhong, Z., Zeng, L., Zheng, J.: A new

872   portable instrument for online measurements of formaldehyde: from ambient to mobile emission

873   sources. Environ. Sci. Technol. Lett, 7, 292-297, https://dx.doi.org/10.1021/acs.estlett.0c00169, 2020.

874 Zou, Y., Deng, X. J., Zhu, D., Gong, D. C., Wang, H., Li, F., Tan, H. B., Deng, T., Mai, B. R., Liu, X. T.,

875   and Wang, B. G.: Characteristics of 1 year of observational data of VOCs, NOX and O3 at a suburban

876   site in Guangzhou, China. Atmos. Chem. Phys., 15, 6625-6636, https://doi.org/10.5194/acp-15-6625-

877   2015, 2015.

878